

X-650-64-204

TM X-55070

FACILITY FORM 808

[REDACTED]

N 65 32114

(ACCESSION NUMBER)

(THRU)

56

(PAGES)

1

(CODE)

TMX 55070

(NASA CR OR TMX OR AD NUMBER)

30

(CATEGORY)

# THE INFRARED INTERFEROMETER SPECTROMETER EXPERIMENT (IRIS)

## (VOLUME I—MARTIAN FLY-BY MISSION)

JULY 1964

GPO PRICE \$ \_\_\_\_\_

CSFTI PRICE(S) \$ \_\_\_\_\_

Hard copy (HC) \$300

Microfiche (MF) 50¢

ff 653 July 65



### GODDARD SPACE FLIGHT CENTER

### GREENBELT, MARYLAND

[REDACTED]

THE INFRARED INTERFEROMETER SPECTROMETER EXPERIMENT  
(IRIS)

by

R. A. Hanel, Goddard Space Flight Center,  
and  
L. Chaney, University of Michigan

GODDARD SPACE FLIGHT CENTER  
Greenbelt, Maryland

RECEIVED NASA OFFICE and  
NASA GUMPERT UNIT

## ACKNOWLEDGEMENTS

In addition to the experimenters, the following people made substantial contributions to the effort presented here:

Frank Bartko, Goddard Space Flight Center

Fred Bartman, University of Michigan

Lawrence Byrne, Goddard Space Flight Center

Grady Nichols, Goddard Space Flight Center

Dr. David Wark, United States Weather Bureau

## CONTENTS

	<u>Page</u>
1. SCOPE . . . . .	1
2. SCIENTIFIC OBJECTIVES . . . . .	1
2.1 <u>THE THERMAL EMISSION SPECTRUM</u> . . . . .	1
2.2 <u>ATMOSPHERIC COMPOSITION</u> . . . . .	4
2.3 <u>ATMOSPHERIC STRUCTURE</u> . . . . .	11
2.4 <u>SURFACE STUDIES</u> . . . . .	14
2.5 <u>ADDITIONAL INVESTIGATIONS</u> . . . . .	17
3. THE INTERFEROMETER SPECTROMETER . . . . .	19
3.1 <u>THEORY OF FOURIER SPECTROSCOPY</u> . . . . .	19
3.2 <u>MECHANICAL AND ELECTROMECHANICAL DESIGN</u> . . . . .	24
3.3 <u>OPTICAL DESIGN</u> . . . . .	26
3.4 <u>ELECTRONIC DESIGN</u> . . . . .	27
3.5 <u>SIGNAL-TO-NOISE RATIO</u> . . . . .	31
3.6 <u>AUXILIARY MEASUREMENTS</u> . . . . .	36
4. DATA REDUCTION . . . . .	37
4.1 <u>SYNTHESIS</u> . . . . .	37
4.2 <u>ANALYSIS</u> . . . . .	38
5. INSTRUMENT CALIBRATION . . . . .	38
5.1 <u>PRIMARY CALIBRATION</u> . . . . .	39

CONTENTS (Continued)

	<u>Page</u>
5.2 <u>CALIBRATION CHECKS DURING ENVIRONMENTAL TESTS</u> . .	39
5.3 <u>CHECK OF CALIBRATION IN THE LAUNCH AREA AND ON LAUNCH PAD</u> . . . . .	40
5.4 <u>CHECK OF CALIBRATION DURING INTERPLANETARY FLIGHT</u> . . . . .	40
5.5 <u>CALIBRATION AT PLANETARY ENCOUNTER</u> . . . . .	40
6. MISSION PROFILE . . . . .	40
6.1 <u>PLANETARY TRANSFER</u> . . . . .	40
6.2 <u>PLANETARY ENCOUNTER MODE</u> . . . . .	41
6.3 <u>OTHER EXPERIMENT CONSIDERATIONS</u> . . . . .	41
7. EXPERIMENT-SPACECRAFT INTERFACE . . . . .	43
Design Parameters for Infrared Interferometer . . . . .	45
REFERENCES . . . . .	47

## ILLUSTRATIONS

<u>Figure</u>		<u>Page</u>
1	Radiative Equilibrium Temperatures in a Simulated N <sub>2</sub> -CO <sub>2</sub> Atmosphere with Trace Amounts of Water . . . . .	3
2	Low-Resolution Thermal Spectra Calculated for Temperature Profiles Shown in Figure 1 . . . . .	5
3	Infrared Spectra of Possible Constituents of the Martian Atmosphere . . . . .	7
4	Transmission of a Synthetic Atmosphere of the Expected Amount of CO <sub>2</sub> (55m atm) and Water Vapor (14 precipitable microns) and the Upper Limits of N <sub>2</sub> O and CH <sub>4</sub> . . . . .	9
5	Cross-Correlation Function of the Spectrum of Water Vapor and a Combination of Water Vapor plus Random Noise with a Signal-to-Noise Ratio of Unity . . . . .	10
6	Transmission Function of CO <sub>2</sub> in Selected Spectral Intervals in the 15μ Band . . . . .	12
7	Weighting Functions Indicating the Pressure Range from Which Thermal Emission Originates . . . . .	13
8	Emissivity in the Infrared of Rock Samples . . . . .	15
9	Emissivity in the Infrared of Quartz and Quartz Sand of Different Grain Size . . . . .	16
10	Schematic Operation of Michelson Interferometer . . . . .	20
11	Schematic Diagram of Interferometer Cube, Mirror Drive System, and Detector Assembly . . . . .	20
12	Interferometer Electronics, Block Diagram . . . . .	28
13	Difference in Spectral Radiance of a Target Colder Than the Interferometer . . . . .	34

ILLUSTRATIONS (Continued)

<u>Figure</u>		<u>Page</u>
14	Difference in Spectral Radiance of a Target Warmer Than the Interferometer . . . . .	35
15	Spacecraft-Experiment Interface . . . . .	44

TABLES

<u>Table</u>		<u>Page</u>
1	Summary of Assumptions Made in the Calculations of Temperatures for the Five Cases Shown in Figure 1 . . . . .	2

## 1. SCOPE

The purpose of this report is

- to show how significant information on the atmosphere and surface of Mars can be extracted from the thermal-emission spectrum of the planet
- to describe the design of an infrared interferometer capable of measuring the thermal-emission spectrum
- to document requirements and constraints of the infrared interferometer experiment on a planetary fly-by spacecraft

## 2. SCIENTIFIC OBJECTIVES

The objective of the infrared interferometer spectrometer (IRIS)\* experiment is to obtain information on the composition and structure of the atmosphere and surface of the planet Mars. This information will be extracted from the thermal-emission spectrum within the interval of  $2000\text{ cm}^{-1}$  (5 microns) to  $500\text{ cm}^{-1}$  (20 microns) and possibly to  $300\text{ cm}^{-1}$  (33 microns) with a spectral resolution of  $5\text{ cm}^{-1}$ . The IRIS experiment is deliberately aimed at a wide spectral range to permit clear identification of many predictable spectral features and, even more important, to allow a search for unexpected phenomena. For a nominal fly-by distance of 5000 km, the resolved area will be a circle of 250-km diameter, approximately equivalent to the resolution now obtained by photographic techniques with ground-based telescopes.

The wide spectral range of the instrument, combined with the relatively high spectral resolution, makes a variety of scientific studies possible; these can be grouped into investigations concerning the atmosphere, and those concerning the planetary surface. In addition, many other inferences can be made from the results of the measurements. The following discussions indicate the wide scope of scientific investigations made possible by this experiment.

### 2.1 THE THERMAL-EMISSION SPECTRUM

The thermal-emission spectrum of a planetary atmosphere depends on many parameters, of which the most important are the temperature profile, the surface temperature and emissivity, the concentration of atmospheric constituents, and the surface pressure. Under the condition of radiative equilibrium, the temperature profile is completely defined by the parameters mentioned above

---

\*IRIS is the Greek word for rainbow.

as well as the solar zenith angle. In theory, if a greater number of measurements of the specific intensity are obtained than the unknown parameters which exist, then all parameters influencing the thermal-emission spectrum can be determined; however, the measurements must be made in independent spectral regions or at different zenith angles. In practice, the extraction of individual parameters is more difficult, and within the limited accuracy of the instruments, different parameters can be determined only within certain limits.

To study the influences of the various parameters on the thermal-emission spectrum and to see how these parameters can be determined from the measurements, some preliminary calculations have been made (Figure 1, Table 1).

Table 1

Summary of Assumptions Made in the Calculations of Temperatures for the Five Cases Shown in Figure 1

Case	1	2	3	4	5
Solar zenith angle	0°	60°	60°	60°	night
Surface temperature (degrees Kelvin)	320°	270°	270°	270°	200°
Surface pressure (atmospheres)	.01	.01	.03	.03	.01
CO <sub>2</sub> concentration	.25	.25	.10	.25	.25
H <sub>2</sub> O concentration	.4·10 <sup>-6</sup>				
Surface emissivity	1	1	1	1	1
Surface reflection for near-infrared	.25	.25	.25	.25	.25

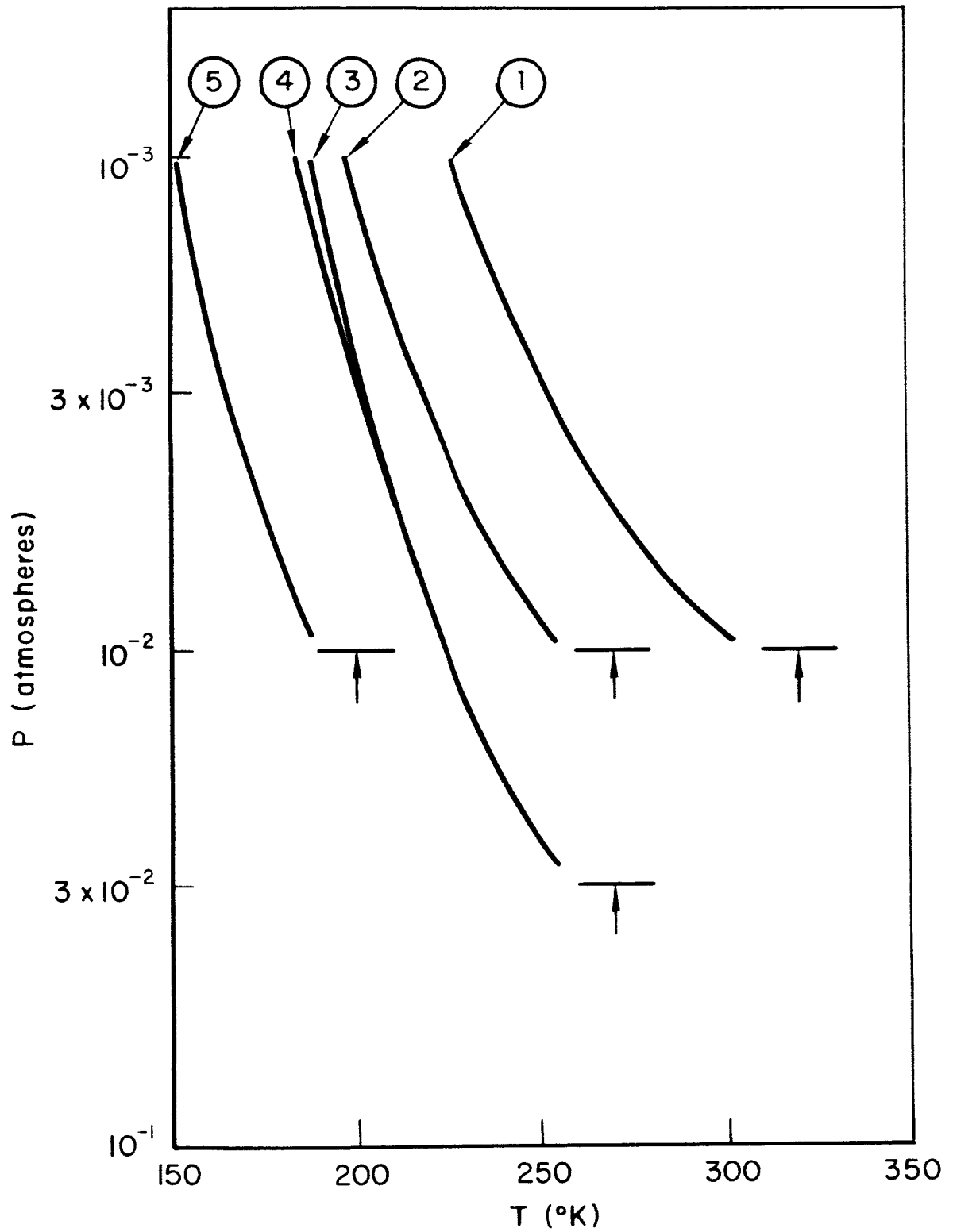


Figure 1—Radiative Equilibrium Temperatures in a Simulated  $\text{N}_2\text{-CO}_2$  Atmosphere with Trace Amounts of Water

The radiative equilibrium temperature distribution for a simulated Martian atmosphere has been calculated, using the technique described in Reference 1. Some cases are shown in which the temperature distributions require modification due to convective energy transport. Five individual cases were studied:

- Case 1 corresponds to the estimated maximum conditions which could possibly occur near the subsolar point. The surface temperature was assumed to be 320°K, slightly above the maximum measured from the earth in the atmospheric window. The calculated temperature profile is shown in Figure 1.
- Case 2 corresponds to the expected nominal condition in the late afternoon local Martian time and  $\pm 45^\circ$  latitude.
- Cases 3 and 4 have been calculated for higher surface pressures.
- Case 5 is representative of the coldest conditions expected during the Martian night.

All calculations were carried out for an  $N_2$ - $CO_2$  atmosphere with trace amounts of  $H_2O$ . Other gaseous constituents that may be detected (by techniques described later) may influence the equilibrium temperatures, and will have to be considered in addition to the  $CO_2$  and the small amount of water vapor. Furthermore, these calculations assume only pressure broadening of the spectral lines. In the low-pressure conditions to be expected on Mars, Doppler broadening will be an important factor and must be considered in a more refined treatment.

Figure 2 shows the corresponding thermal spectra. The spectral resolution of the diagram is very low, varying between approximately 50 and 100 wavenumbers in the most interesting portions. The abscissa is proportional to the fraction of the energy available from a blackbody at 270°K. The wavenumber and the wavelength scales are nonlinear. The strong 15-micron  $CO_2$  band dominates the central part in all spectra. Although the temperature profiles of Cases 3 and 4 are almost the same, the higher abundance of  $CO_2$  in Case 4 causes lower temperatures in the 15-micron band. A comparison between Cases 2 and 4 clearly show the strong influence of the surface pressure, evidence that the surface pressure may be extracted from the emission spectrum.

## 2.2 ATMOSPHERIC COMPOSITION

Identification of gases known to be present in the Martian atmosphere ( $CO_2$ ,  $H_2O$ ) and estimates of their abundances are among the objectives of the IRIS experiment. But an even more important objective is the possible detection, as well

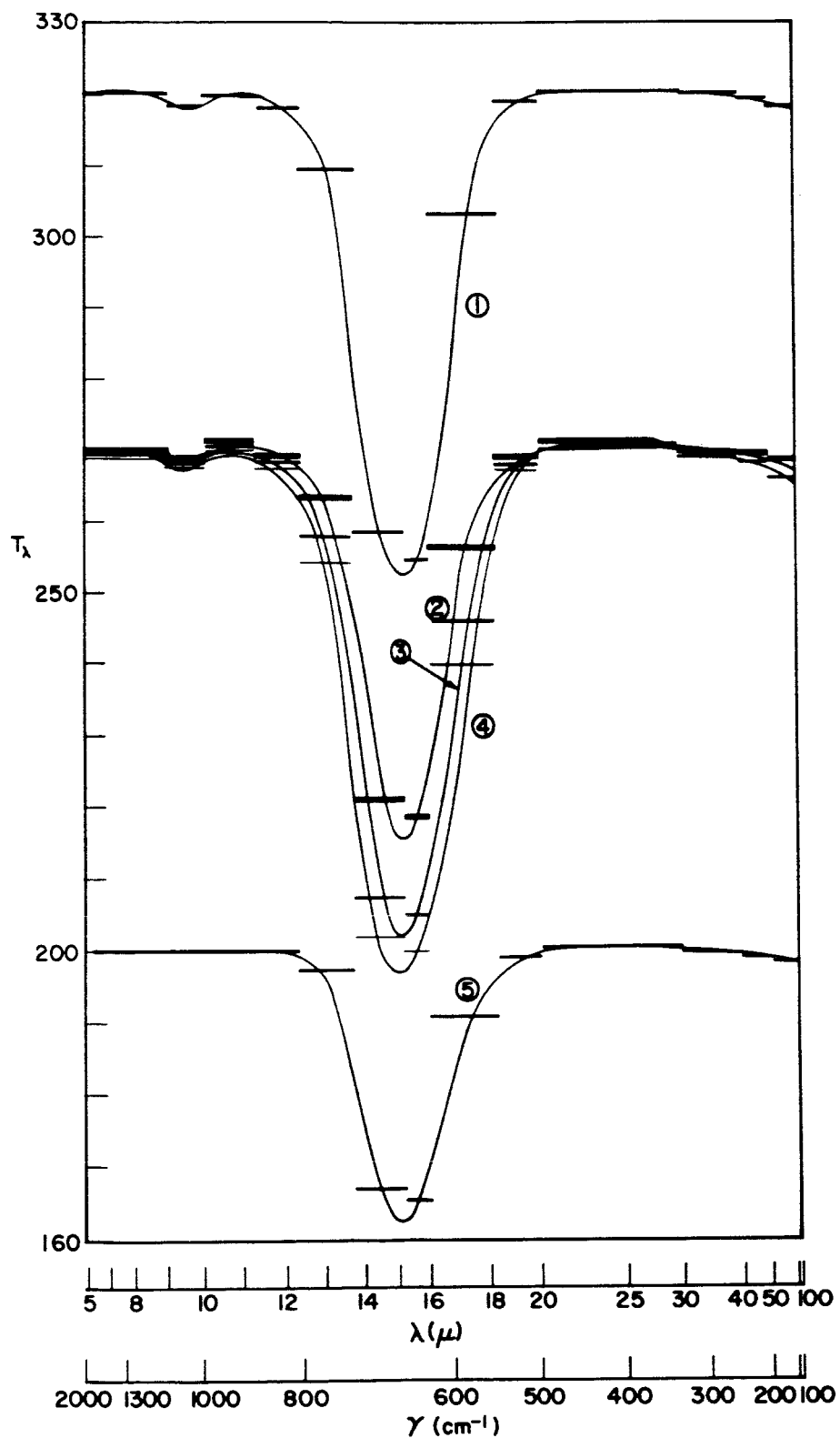


Figure 2—Low-Resolution Thermal Spectra Calculated for Temperature Profiles Shown in Figure 1

as the establishment of better upper limits, of yet unidentified but suspected constituents ( $\text{N}_2\text{O}$ ,  $\text{NO}$ ,  $\text{NO}_2$ ,  $\text{CH}_4$ ,  $\text{C}_2\text{H}_4$ ,  $\text{C}_2\text{H}_6$ ,  $\text{NH}_3$ ,  $\text{O}_3$ ).

The identification of gases is based on the characteristic absorption spectrum of each gas. Gases in the atmosphere absorb thermal radiation from the surface and, according to Kirchhoff's law, re-emit blackbody radiation as determined by their own temperature. As most atmospheric temperatures will be somewhat lower than surface temperatures, the atmospheric spectra will appear as absorption spectra. However, this is not necessarily true under all conditions; for example, under the condition of a strong temperature inversion in the atmosphere, or in spectral regions where the surface emissivity is low, a reversal may take place and the spectrum of a gas may appear in emission. These complications do not exist in the interpretation of spectra in the visible or near-infrared (say below 2 microns) where thermal emission is negligible compared to reflected solar radiation.

The long-wave infrared spectra may be more difficult to interpret, and the theory of radiative transfer must be used extensively in a proper treatment of the long-wave spectra; but the thermal-emission spectra yield additional information, such as the temperature profile, which will be discussed later. Furthermore, many atmospheric constituents which might be of biological interest, such as  $\text{CH}_4$ , are relatively complex molecules which show strong vibrational and rotational bands in the middle and far infrared but very little detectable absorption phenomena in the visible part of the spectrum. For these reasons, the analysis of atmospheric constituents in the far infrared is extremely interesting in spite of the difficulties associated with their interpretation.

Figure 3 shows the spectra of constituents which may be expected in the atmosphere of Mars. The spectra are drawn schematically only, without the many details which can be recognized with a resolution of 5 wavenumbers. The abundance of the gases was taken according to the upper limits presently accepted (Kuiper, 1952; Sinton, 1961)\*. The optical depth is shown on a relative scale.

The broad wings of the bands shown in Figure 3 correspond to the absorption continuum arising from the sum of the wings of all individual lines in the band. The situation for the Lorentz line shape is shown. This must be considered an upper limit for a number of reasons: First, as Benedict has shown, the Lorentz shape does not strictly apply far away from the line centers; second, and more important, Doppler broadening will be an important factor which causes a much

---

\*References 2 and 3

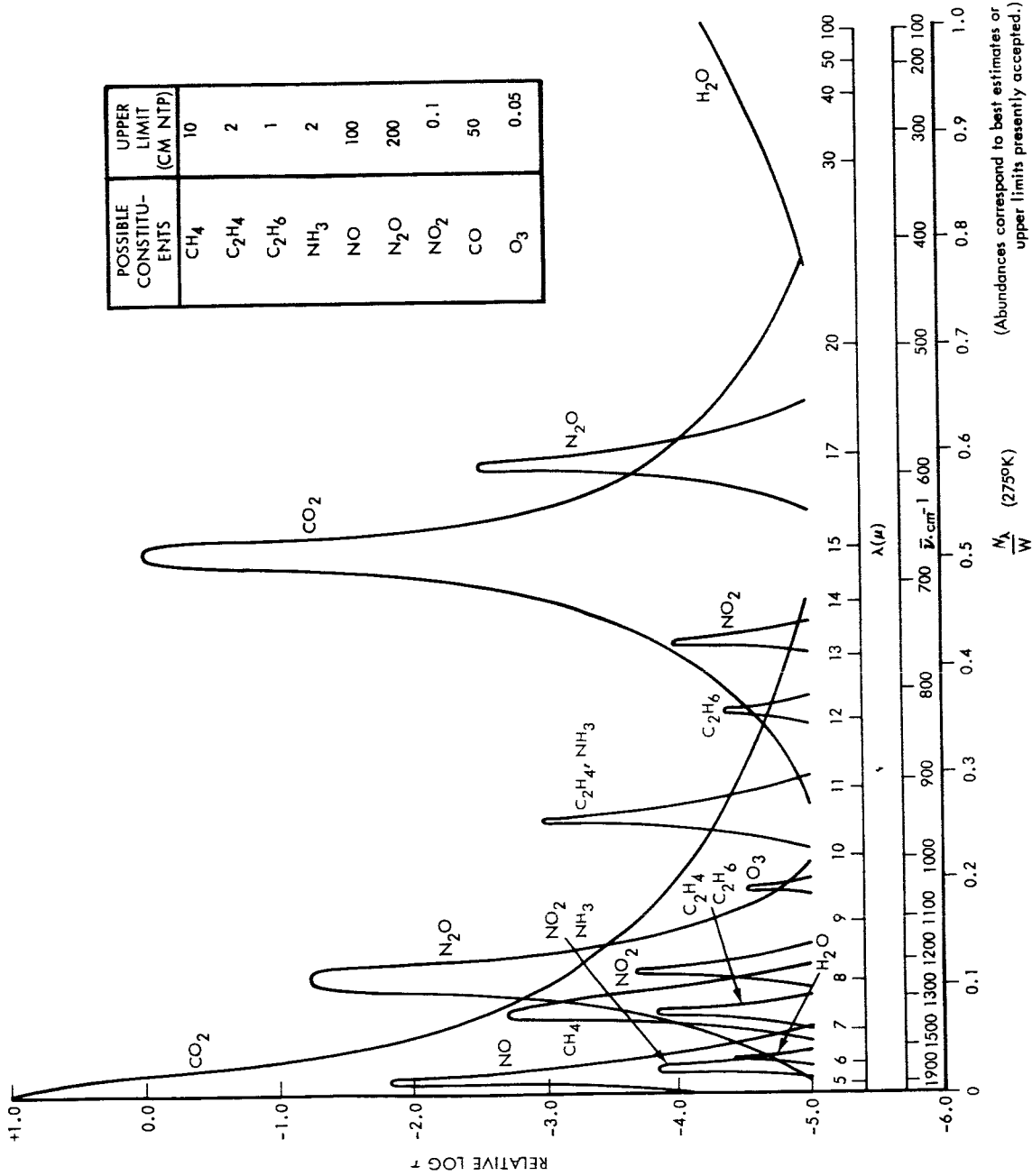


Figure 3—Infrared Spectra of Possible Constituents of the Martian Atmosphere

faster decay of the line shape away from the line center and consequently gives rise to a much weaker continuum than that indicated. The 15-micron  $\text{CO}_2$  band and the  $\text{N}_2\text{O}$  band near 8 microns, using the above upper limits and measured band intensities, are strong enough to be totally opaque. Methane ( $\text{CH}_4$ ) and other hydrocarbons ( $\text{C}_2\text{H}_4$ ) may also be detected. Water vapor, ozone, and others are more difficult to extract from the spectra. But, because water vapor is extremely important both from an atmospheric-physics and from a biological viewpoint, a technique for the possible identification of this as well as other less abundant constituents will be described here.

Water vapor has strong vibration-rotation bands near 6.3 microns and the rotational band beyond 20 microns. If the spectral response of the instrument is restricted to 20 microns, then only the first bands are available for analysis. Figure 4 shows the transmission of a synthetic atmosphere consisting of the expected amount of  $\text{CO}_2$  and water vapor, in the full detail to which the spectra can be generated by the interferometer. In addition, the figure shows spectral transmission of  $\text{CH}_4$  and  $\text{N}_2\text{O}$ , both present in a quantity corresponding to the presently accepted upper limit, and under the expected average atmospheric conditions. As can be seen, the atmosphere is nearly opaque between 600 and 750 wavenumbers (15-micron  $\text{CO}_2$  band) and near 1300 ( $\text{N}_2\text{O}$ ). Water vapor shows absorption phenomena between about 1300 and 2000 wavenumbers. Even in the strongest parts, the maximum absorption does not exceed a few percent. Consequently, it will be difficult to recognize the presence of water vapor in this band, and even more difficult to determine the abundance quantitatively. Fortunately, however, the water-vapor band spreads over almost 700 wavenumbers and shows considerable structure. This feature allows the use of statistical methods to obtain information about water vapor from the almost 140 individual spectral data points derived from a single interferogram. The cross-correlation function of the received spectrum and the known spectrum of water vapor is obtained by

$$C_{(x)} = \int I_{\nu} W_{(\nu+x)} d\nu .$$

Even under conditions of severe noise, the cross-correlation function shows a maximum for  $x = 0$ . The correlation technique is a powerful tool for recognizing and estimating the amount of particular constituents in a complicated and possibly noisy spectrum. Figure 5 shows a sample of a cross-correlation function of the water-vapor spectrum with a combination of random noise and water vapor (signal-to-noise ratio equal to one). The same technique may also be employed to assess the amounts or upper limits for other atmospheric constituents.

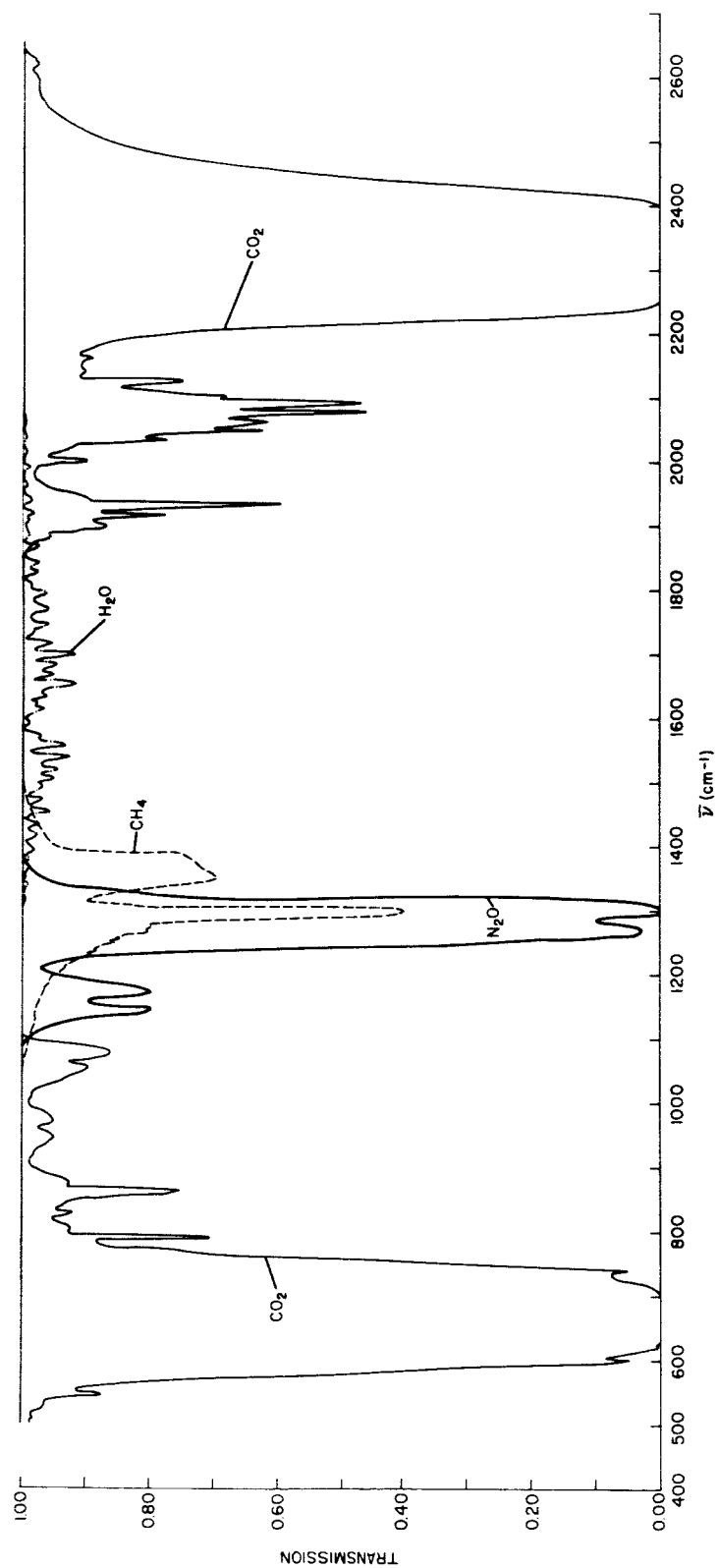


Figure 4--Transmission of a Synthetic Atmosphere of the Expected Amount of  $\text{CO}_2$  (55m atm) and Water Vapor (14 precipitable microns) and the Upper Limits of  $\text{N}_2\text{O}$  and  $\text{CH}_4$

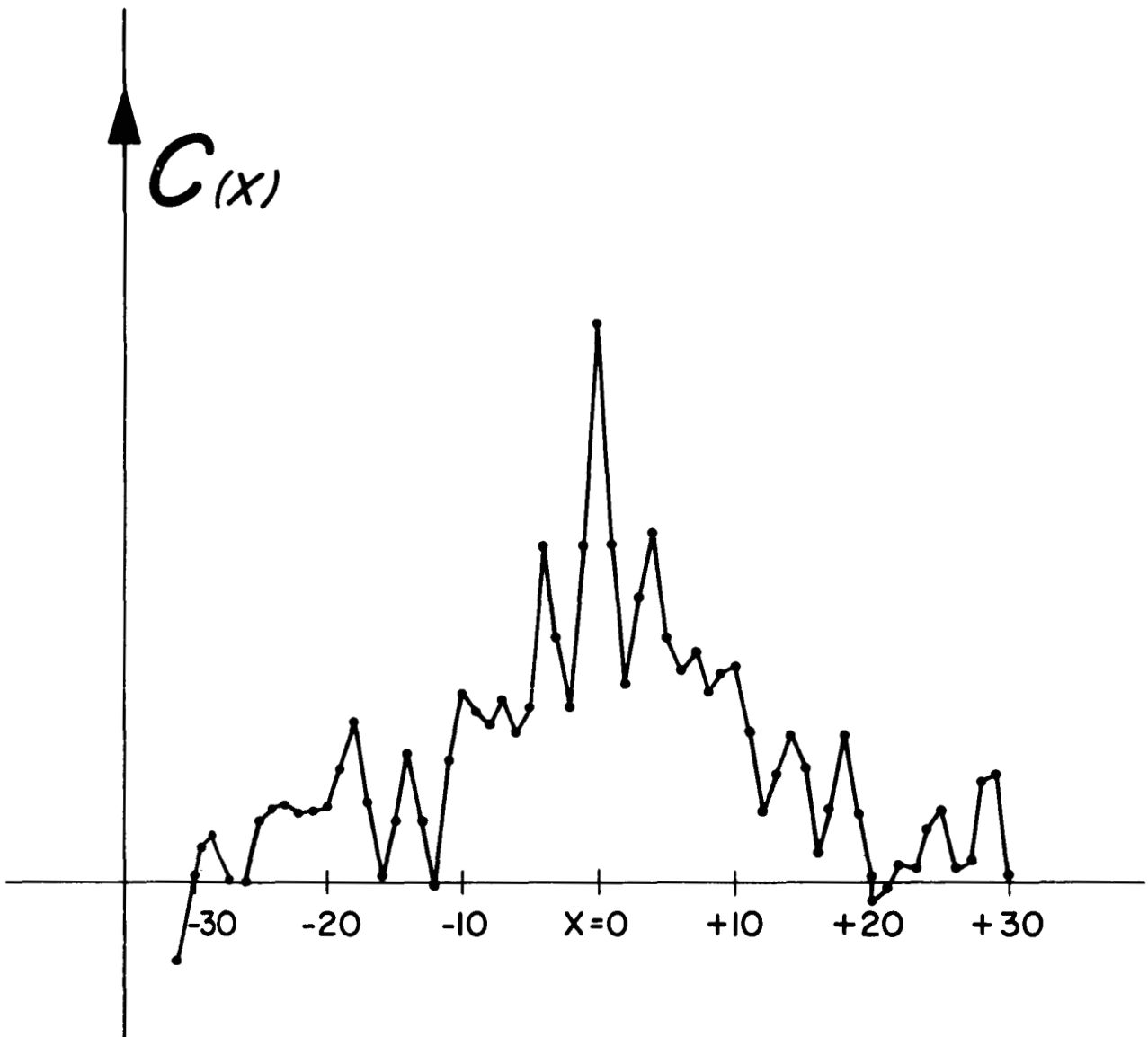


Figure 5—Cross-Correlation Function of the Spectrum of Water Vapor and a Combination of Water Vapor plus Random Noise with a Signal-to-Noise Ratio of Unity

### 2.3 ATMOSPHERIC STRUCTURE

Use of satellite-measured radiation values to determine the atmospheric temperature distribution of the earth's atmosphere has been discussed by Kaplan (1960), Wark (1961), Yamamoto (1961), King (1963), and Fleming, et al. (1964).\*

Temperature distribution in the atmosphere is related to the absorption characteristics and the upward radiance through the radiative transfer equation expressed, for example, in terms of the pressure. In the spectral region of strongest absorption, the atmospheric emission arises from the upper portion of the atmosphere. Radiation in spectral regions of weaker absorption originates from lower layers in the atmosphere. Similar considerations can be applied to the extraction of the temperature distribution of the Martian atmosphere.

To illustrate, Figure 6 shows the transmission in selected spectral intervals within the  $15\mu$  carbon dioxide band. The transmission data were provided by Wark and Yamamoto. The transmission curves are based upon unpublished laboratory measurements (Yamamoto, Sasamori, Wark and Moore abstract in Publication IAMAP No. 13 on the XIIIth General Assembly of the IUGG, 1963) which assumed that the total amount of  $\text{CO}_2$  was 5500 cm atmospheres, and the surface pressure 10 mb (Kuiper, 1964)<sup>†</sup> which corresponds approximately to the expected conditions on Mars.

Temperature corrections were made in the same manner as in the Meteorological Satellite Laboratory (USWB) reports #10 and #21, using a Mars model atmosphere to calculate effective temperatures  $T_e$  (surface temperature 270°K, adiabatic lapse rate to 6.5 mb, radiative equilibrium to 1 mb, extrapolation above.)

Figure 7 shows the atmospheric zones contributing to the outgoing radiance which can be detected by the probe. Lorentz broadening only was taken into account; this approach is inaccurate, especially at the lower atmospheric pressures. In general, a somewhat greater absorption will be found than that shown, but the differences will be very small in all but the intervals of greatest absorption. Figure 7 demonstrates that the radiance values recovered by the interferometer allow a determination of the temperature profile. As the interferometer resolution is  $5\text{ cm}^{-1}$  over the whole band, redundant measurements are available which increase the accuracy of the temperature determination.

---

\*References 4, 5, 6, 7, and 8

† Reference 9

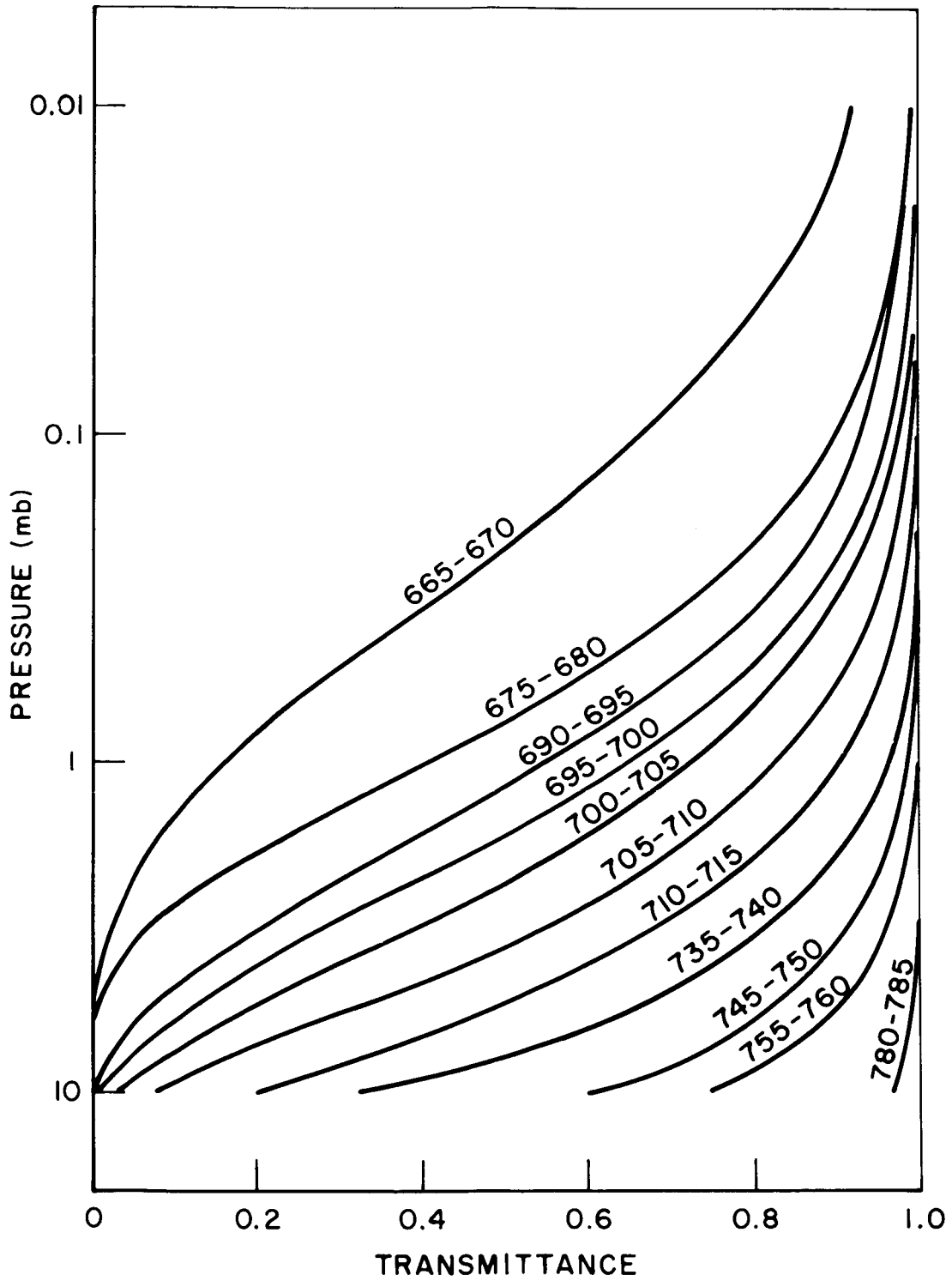


Figure 6—Transmission Function of CO<sub>2</sub> in Selected Spectral Intervals in the 15 μ Band (after D. Q. Wark and G. Yamamoto)

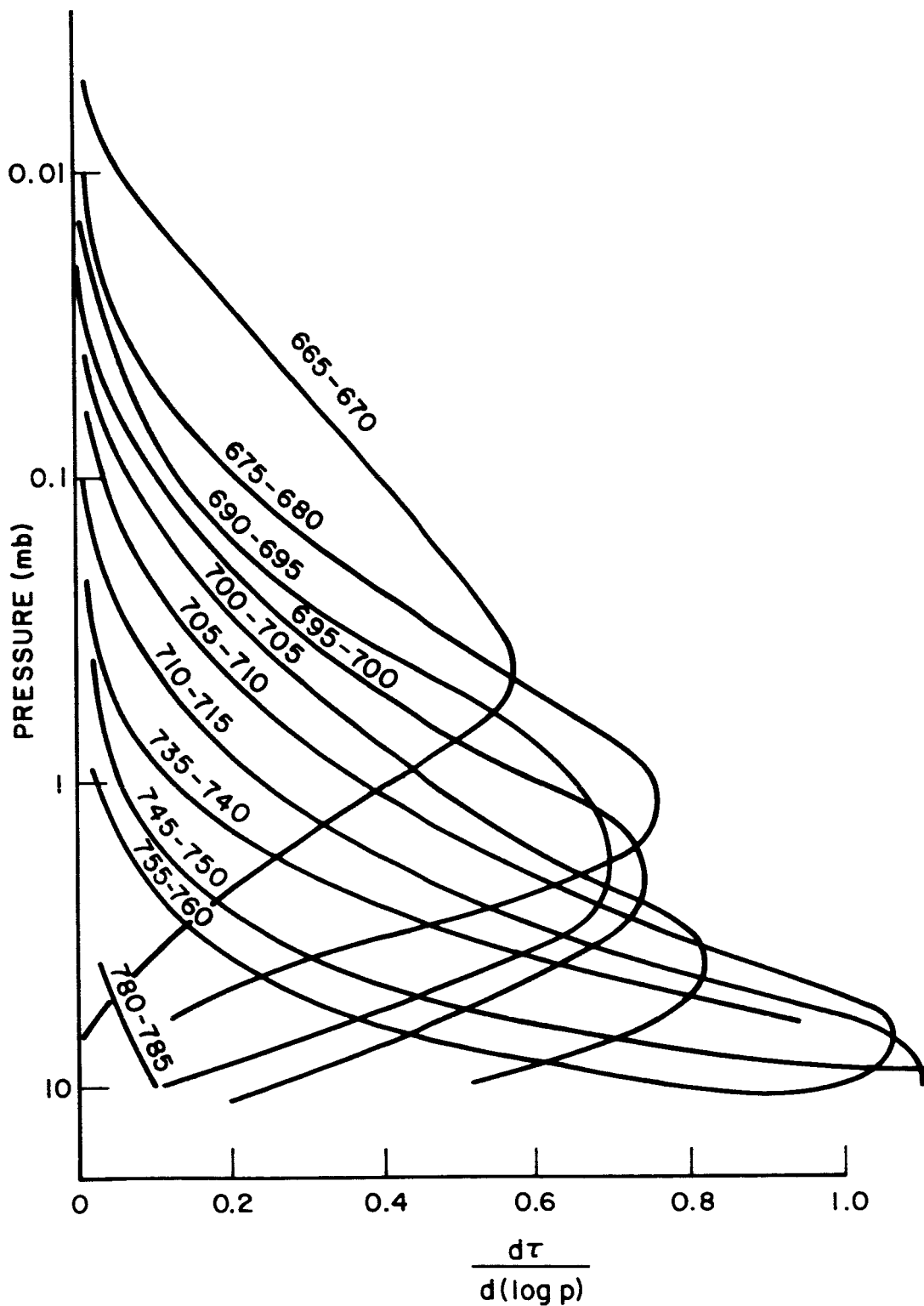


Figure 7—Weighting Functions Indicating the Pressure Range from Which Thermal Emission Originates (after D. Q. Wark and G. Yamamoto)

## 2.4 SURFACE STUDIES

After the atmospheric constituents are identified, the effect of atmospheric absorption can be removed from the spectrum in those spectral ranges where the atmosphere is not opaque. The specific intensity emitted by the surface in the non-opaque regions is then obtained,

$$I_{\nu}(\text{surface}) = \epsilon_{\nu} B_{\nu}(T_{\text{surface}}).$$

In the far infrared, most natural surfaces known on earth (rocks, gravel, plants, snow, etc.) have a high emissivity over large spectral ranges. However, the crystalline structure of minerals and the structure of complex molecules create stretching and bending resonances. For example, quartz exhibits strong stretching bands between 800 and 1100  $\text{cm}^{-1}$  caused by the Si-O bond; other stretching groups (Si-Si) appear between 600 and 800  $\text{cm}^{-1}$ . The same mineral has a bending mode (Si-O-Si) at 430 to 460  $\text{cm}^{-1}$ . These resonances give a pronounced rise in the infrared reflectivity which can best be observed on polished samples. The increase in reflectivity is necessarily associated with a reduction in emissivity over the same spectral range.

The sharp rise in reflectivity has been well known since the early days of infrared studies. Rubens used the selective reflectivity of quartz plates to isolate narrow spectral bands in the far infrared. The reststrahlen phenomenon depends somewhat on the temperature of the sample and to a much higher degree on the surface roughness. Lyon (1963)\* has studied the emission and reflection spectra of many minerals in great detail. The emissivity of several rocks in solid but unpolished form can be judged from Figure 8. Polished samples show an even stronger reststrahlen effect. Grooves on a rough surface act as small cavities and increase the emissivity considerably. Similar phenomena can be recognized in the sandy or powdered form, as shown in Figure 9. Fine dust of a particle size below 1 micron loses the reststrahlen effect almost completely, and the surface emits almost with the characteristics of a graybody or possibly even a blackbody. Scattering effects also become important for these particle sizes. For a grain the size of fine sand, approximately 25 to 50 microns, the reststrahlen phenomenon is weak, but the identification of the material may still be possible, as has been demonstrated also by Bell and Eisner (1956).† Identification of the mineralogical composition of the Martian surface by the thermal-emission spectrum is, therefore, very promising, except for areas where fine dust may cover a large portion of the surface. Such areas may exist on Mars, but other

---

\*Reference 10

† Reference 11

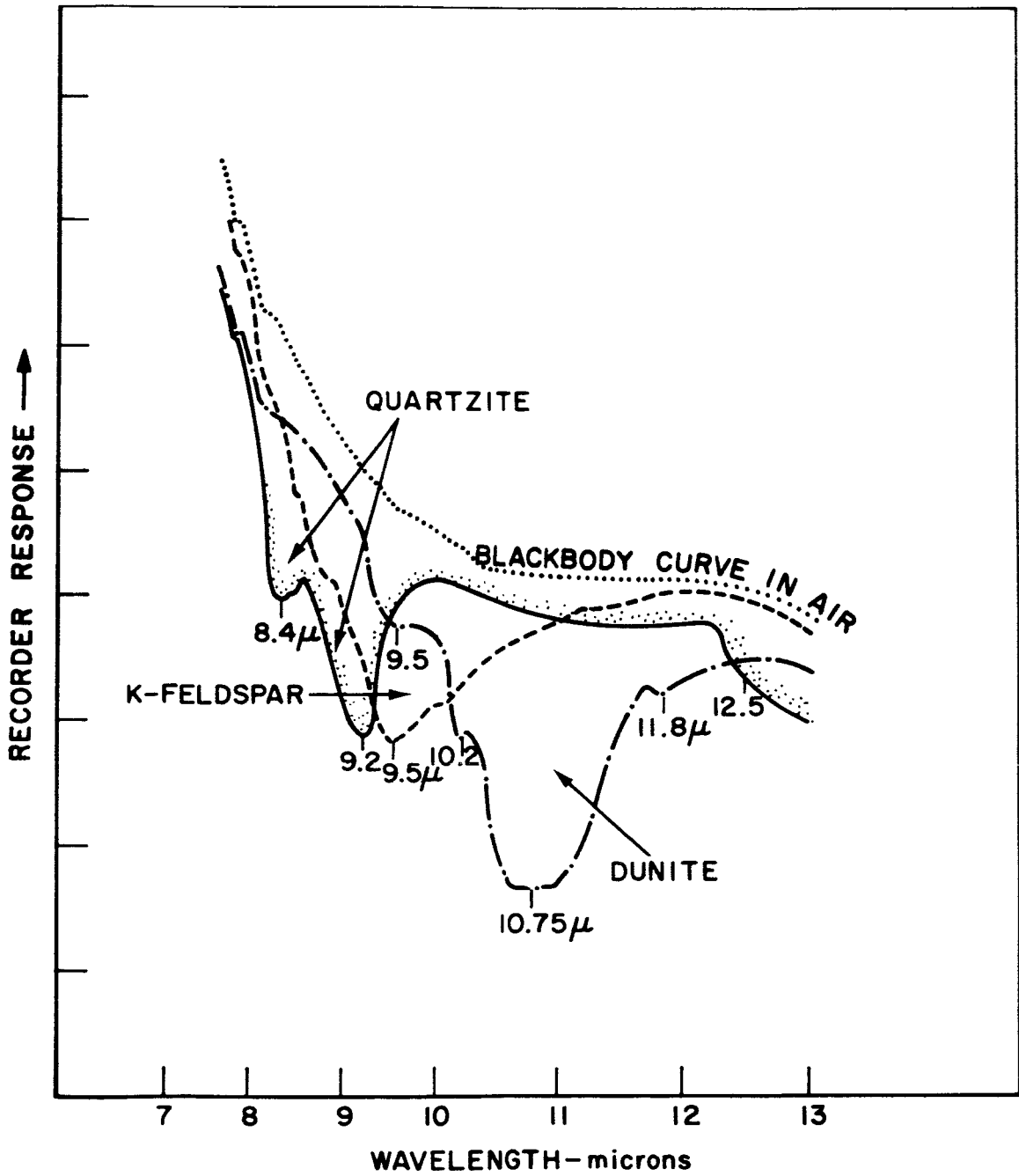


Figure 8—Emissivity in the Infrared of Rock Samples (after Lyon)

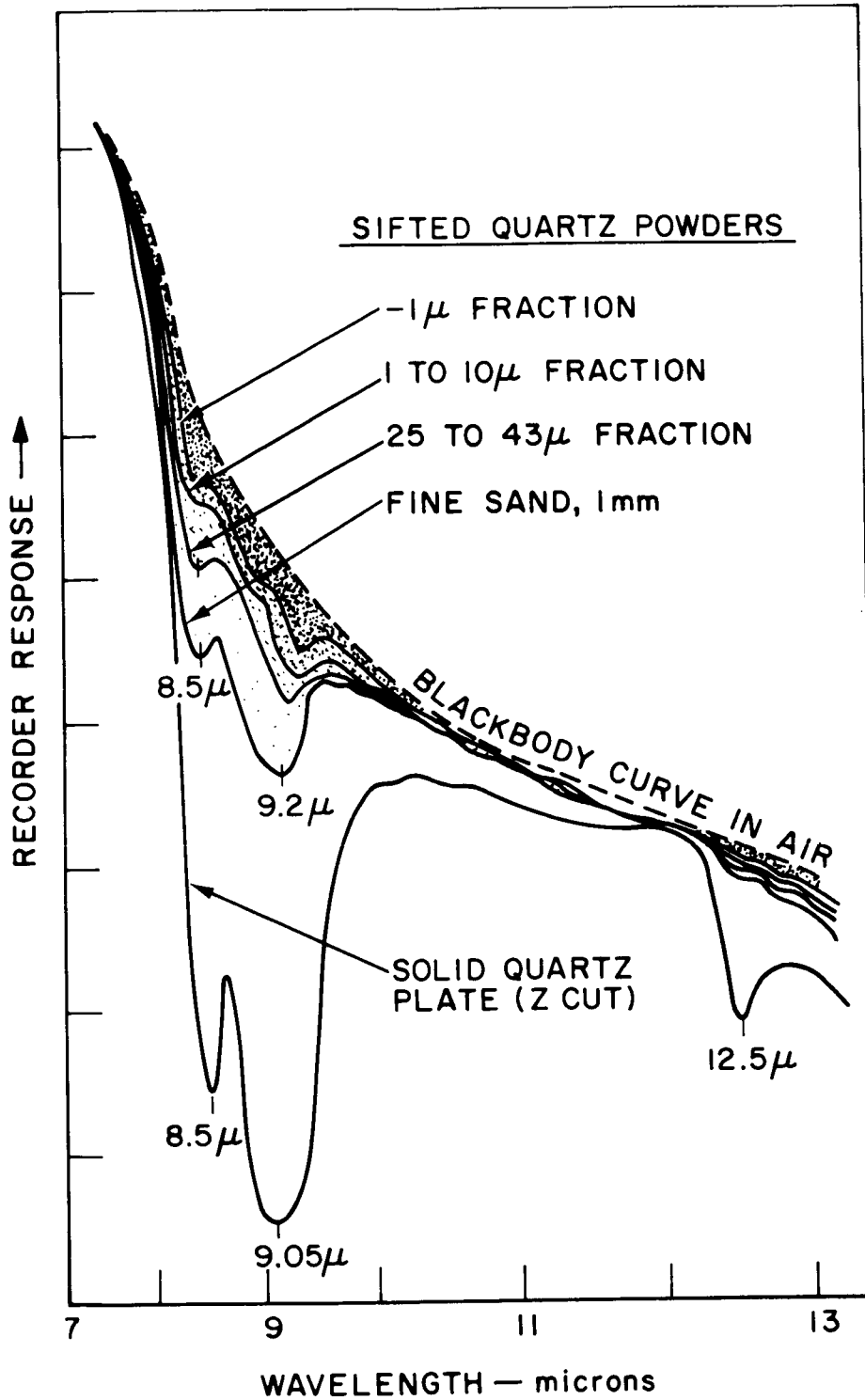


Figure 9—Emissivity in the Infrared of Quartz and Quartz Sand of Different Grain Size (after Lyon)

areas may expose more solid rocks or gravel or coarse sand. Winds may sweep highlands clear of the finer particles and dust may accumulate in the valleys. The appearance of a pronounced reststrahlen effect would not only allow identification of a particular mineral, but would also be indicative of a coarse surface structure.

The surface emission spectrum may also yield important information on the existence of other chemical substances of inorganic, or possibly even organic, nature if they occur in a sufficiently high concentration. The Sinton bands near  $3.5\mu$ , although outside the spectral range of this experiment, are a typical example of unexpected (and so far unexplained) spectral features. The search for reflection or absorption phenomena is especially interesting if the spatial resolution allows measurements in predominantly bright and predominantly dark areas.

A broad program of laboratory and field measurements on earth is an indispensable requirement for proper interpretation of planetary emission spectra. The engineering model of the interferometer under construction will be used for experimental studies in this area.

## 2.5 ADDITIONAL INVESTIGATIONS

In addition to the generally well defined tasks already mentioned, a number of inferences may be derived directly or indirectly from the spectra:

- Chemistry of the atmosphere and surface  
Chemical equilibrium between identified gases and others can be used to estimate the abundance of unidentified but suspected constituents; the photochemical equilibrium between  $\text{CO}_2$ ,  $\text{CO}$ ,  $\text{O}_2$ , and  $\text{O}_3$  is one example. Furthermore, the atmospheric gases must be in chemical equilibrium with the surface materials.
- Ultraviolet Radiation  
Knowledge of the composition of the atmosphere, especially the  $\text{CO}_2$  content and upper limits for  $\text{O}_3$ , allows calculations of the upper limits of the solar ultraviolet spectrum at the surface of the planet. The ultraviolet radiation at the surface is of biological significance.
- Relative Humidity in the Atmosphere  
The relative humidity near the surface is again of great biological interest. Low temperatures near the morning terminator may allow water vapor to condense in the form of dew or frost; condensation of this nature may be the only source of water available to vegetation if it is present. High temperatures near the subsolar point would cause the water to boil

there. At 10 mb, water boils at +7°C. The relative humidity in the atmosphere also governs the condensation of clouds. Atmospheric regions where water or ice clouds are possible, or likely, can therefore be determined. All these considerations will be greatly aided by theoretical studies of radiative and convective equilibrium conditions in the Martian atmosphere.

- Meteorology

The temperature distribution in the atmosphere and the mode of energy transport are intimately connected. The measured temperature profile will give an indication of atmospheric stability. Lapse rates close to the adiabatic one may indicate a convective layer in the atmosphere (troposphere). Theories on the general circulation, or more concisely the Martian meteorology, are intimately related to the temperature profile.

The temperature-versus-pressure data will also be important in investigating the existence and occasional sudden disappearance of the blue haze. If this phenomenon is associated with condensing or sublimating material, the phase diagram of suggested materials must be consistent with the temperature structure derived by the experiment.

The planning of missions designed to land probes on the surface of Mars will benefit also from a better knowledge of the temperature profile, the atmospheric composition, and the surface pressure.

- Spectral Emissivity and Surface Temperature

Determination of the spectral emissivity allows a more accurate determination of the true surface temperature. Most materials which show residual ray phenomena in certain parts of the spectrum radiate as nearly blackbodies elsewhere. Therefore, the maximum equivalent blackbody temperature determined over a wide spectral range will be closer to the true temperature of the surface than measurements obtained by radiometers covering a wide or narrow spectral interval. A better interpretation will be possible of radiometric data obtained in the atmospheric window from the earth, or of radiometric measurements performed from fly-by spacecraft. However, special care must be taken in interpreting surface temperatures if the surface is covered with very fine powdery material; this situation will require application of the scattering theory of small particles densely packed, which is quite complicated and not well understood today.

- Thermal Inertia of Surface Material

The surface temperature as a function of solar zenith angle, especially near the morning terminator, provides data about the thermal inertia of

the surface material. Calculations similar to those performed for the lunar surface can be applied. The great difference in thermal inertias of loose sand and solid rock provides a tool for distinguishing among various surface conditions.

### 3. THE INTERFEROMETER SPECTROMETER

The instrument, basically a Twyman-Green modification of the Michelson interferometer (Figure 10), departs from the classical laboratory designs in several areas:

- The drive mirror is suspended by a parallel leaf-spring system.
- The mirror assembly is driven by a moving coil in a strong magnetic field; nearly critical damping is provided by electronic means.
- The mirror motion is monitored by an auxiliary interferometer to assure proper sampling times and uniformity in the mirror speed by closed-loop feedback control.
- The compensating plate is moved to a position adjacent to the beam-splitter.

The particular configuration of the interferometer (Figure 11) was chosen because of its inherent compactness, large light-gathering power, and design simplicity.

Radiation arriving within the field of view is divided by the beam-splitter into two components which recombine and interfere after reflections on the fixed and moving mirrors respectively. The recombined beam, focused on the detector, is modulated by the motion of the scan mirror proportional to the speed of the mirror and the wavenumber of the incident radiation. The output signal from the detector, called the interferogram, is the Fourier transformation of the spectrum of the incident radiation. The signal is amplified, digitized, and transmitted over the spacecraft telemetering system. On the ground, the spectrum is reconstructed by applying the inverse transformation. The original spectrum can be precisely reconstructed only within certain limits of accuracy of spectral range and of spectral resolution.

#### 3.1 THEORY OF FOURIER SPECTROSCOPY

Interference spectroscopy, first suggested by Michelson after the development of his original interferometer, was not pursued because of extreme computational

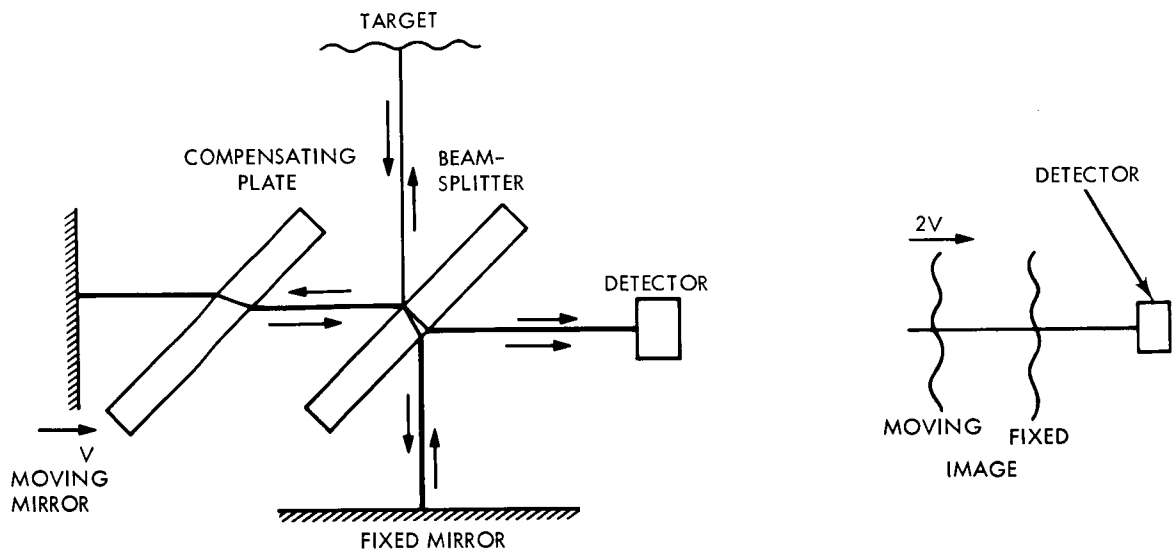


Figure 10—Schematic Operation of Michelson Interferometer

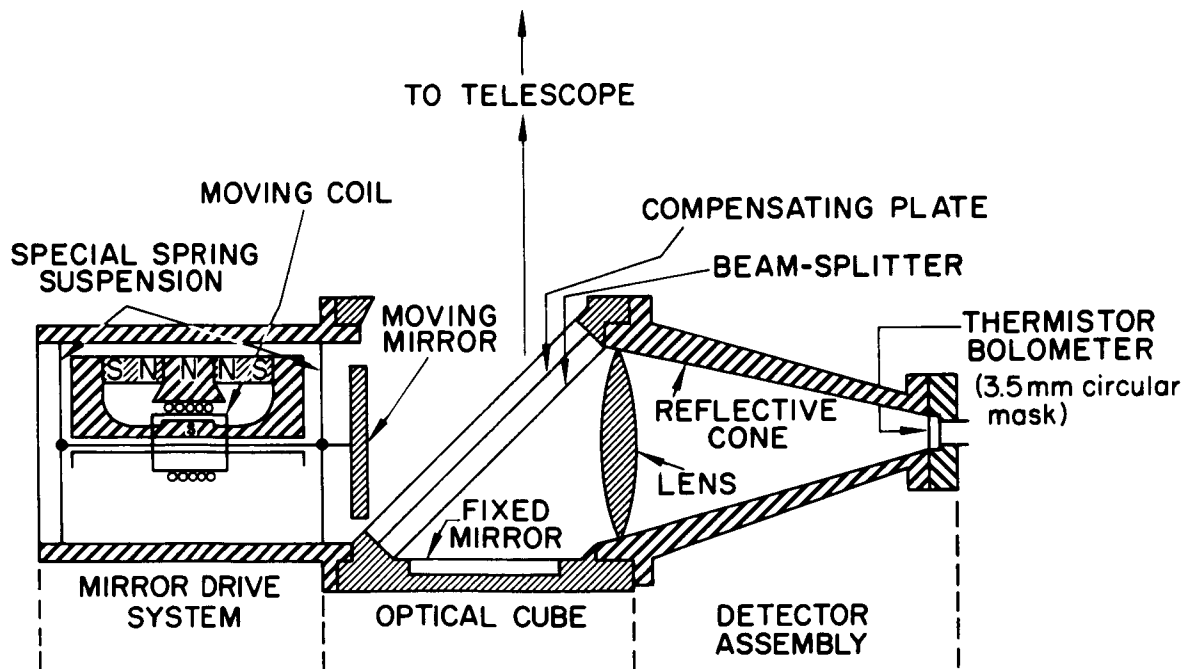


Figure 11—Schematic Diagram of Interferometer Cube, Mirror Drive System, and Detector Assembly (The neon light source and the auxiliary detector for the 5852Å reference line are not shown.)

difficulties, and further development was forced to wait upon the advent of electronics and high-speed digital computers. In the last decade, interference spectroscopy has made great advances; work has been reported by Fellgett (1958), Gebbie (1959), Mertz (1956), Connes (1961), Strong and Vanesse (1958-59), Loewenstein (1963),\* and many others. Excellent summaries may be found in articles by Jacquinet (1960) and by Connes (1961).†

The interferometer is shown schematically in Figure 10; the source of radiation will be an extended source which completely fills the field-of-view with radiation passing through the instrument without collimation. The output fringe pattern of the interferometer is focused on the detector, which is masked to eliminate all but the central fringe. The output of the detector is amplified and recorded as a function of path difference,  $d$ , between the fixed and movable mirror.

The relationship between the effective path difference, the order of interference, and the radiation wavelength is

$$m\lambda = 2d \cos \theta$$

where

$d$  is the path difference between the two interferometer paths (cm)

$m$  is the order of interference

$\lambda$  is the wavelength (cm)

$\theta$  is the angle of an oblique ray through the interferometer.

This expression shows that, for a given monochromatic signal of wavelength  $\lambda$ , the circular fringe corresponding to a given order  $m$  expands away from the center of the pattern as the separation of the mirrors is increased. The detector is mounted behind the mask so that only the central fringe is detected; each spectral element is thereby modulated sinusoidally at a rate inversely proportional to its wavelength. As the source has an appreciable range of spectral elements, the signal detected will be the superposition of many modulated intensities multiplied by a parameter which is the "responsivity" of the

---

\*References 12, 13, 14, 15, 16, 17, and 18

†References 19 and 20

system; i. e.,

$$\phi_{(x)} = \frac{1}{2} \int_0^{\infty} K_{\nu} N_{\nu} d\nu + \frac{1}{2} \int_0^{\infty} K_{\nu} N_{\nu} \cos 2\pi\nu x d\nu$$

where  $N_{\nu}$  is the spectral radiance of the source (assumed to be the same at all parts of the field-of-view)

$\nu$  is the wavenumber,  $\text{cm}^{-1}$  ( $\nu = \frac{1}{\lambda}$ )

$x$  is the instantaneous value of the effective path difference of the two beams of the interferometer (cm)

$K_{\nu}$  is a parameter which expresses the effective spectral responsivity of the interferometer, including the characteristics of the optics, the detector, and the electronic amplifiers

The interferogram is then taken to be

$$\begin{aligned} I_{(x)} &= 2 \left[ \Phi_{(x)} - \frac{1}{2} \Phi(0) \right] \\ &= \int_0^{\infty} K_{\nu} N_{\nu} \cos 2\pi\nu x d\nu , \end{aligned}$$

which is the Fourier cosine transform of  $K_{\nu} \cdot N_{\nu}$ . The product  $K_{\nu} \cdot N_{\nu}$  can be obtained uniquely from the measured interferogram, taking the inverse transform by digital computation. The relationship between  $N_{\nu}$  and the product  $K_{\nu} \cdot N_{\nu}$  will be established by laboratory calibrations; the validity of the laboratory calibrations is established by in-flight calibrations.

The true spectral distribution  $K_{\nu} \cdot N_{\nu}$  is found only when the interferogram is recorded for an infinite range of  $x$ . For a finite range of  $x$ , each spectral component is spread out into a shape known as the instrumental profile. This profile also depends on the obliquity of rays through the interferometer, and thus on the solid angle of the field-of-view. The instrument profile may be modified as desired during computation of the transform; this process, called apodization, usually is done to remove secondary maxima at the expense of resolution.

Including all these effects, the expression for the interferogram becomes

$$I_{(x)} = \int_0^{\infty} N\nu \cdot s(\nu, x) \cdot \cos [2\pi\nu x + \phi(\nu, x)] d\nu ,$$

where

$$S(\nu, x) = s(\nu, x) \exp [i \phi(\nu, x)]$$

is the Fourier transform of the instrument profile (including the parameter  $K_\nu$  mentioned previously).

The spectral distribution is again obtained by computing the Fourier transform of  $I_{(x)}$ . Reconstruction of the spectral distribution of the source  $N_\nu$  is obviously an approximation of the actual spectral distribution. This approximate solution (i.e., the transform of the interferogram) is the convolution of the actual spectral distribution with the instrument profile; therefore, it is mandatory to determine the form of the instrument profile. This can be done experimentally, because the instrument profile is the apparent spectral distribution given by a monochromatic source. This determination of the instrument profile is an important part of the laboratory calibrations.

Two factors which influence the instrument profile and reduce the quality of the data are the limitation arising from the finite path of the movable mirror, and the effect of oblique rays through the interferometer. The resolution limit imposed by the finite-path limitation is

$$R = \nu L \text{ or } \Delta\nu = \frac{1}{L} ,$$

(assuming linear apodization to remove secondary maxima in the instrument function). The resolution limit imposed by oblique-ray effects is

$$R\Omega = 2\pi, \text{ or } \Delta\nu = \frac{\nu\Omega}{2\pi} .$$

In the above,  $R$  is the resolution  $\nu/\Delta\nu$ ,  $L$  is the maximum path difference on either side of zero path difference, and  $\Omega$  is the solid-angle field-of-view of the interferometer.

- Advantages of the Interferometer

An analysis by Jacquinot indicates that, where a source whose spectrum is defined by a radiance  $N_\nu$ , having  $M$  spectral elements of interest, is to be analyzed with a resolution  $R$  in a time  $T$  with an optical system which is detector-noise-limited (as presently in the infrared), then the signal-to-noise ratio is increased by maximizing the time  $t$  of observation of each spectral element, the admissible solid angle  $\Omega$ , and the transmission factor  $\epsilon_\nu$  (the optical efficiency).

An interferometer fulfills these requirements to a high degree. The time of observation is  $t = T(m/M)$ , where  $m$  is the number of spectral elements studied simultaneously. For an interferometer,  $m$  equals  $M$ , and  $m/M$  has the maximum value 1. The luminous energy received by the detector is  $N_\nu \cdot A \cdot \Omega$ . The quantities  $A$  and  $\Omega$  can both be made large for an interferometer, as long as the resolution limitation  $R\Omega = 2\pi$  is not exceeded (for comparison, the same resolution limit for a grating spectrometer is  $R\Omega < 0.1$ ). The transmission factor  $\epsilon$  is the only area where the superiority of the interferometer may be questioned for a given application. The reflectivity and transmissivity of the beam-splitter is of primary importance and it may be difficult to obtain high efficiency from mechanically suitable materials in certain portions of the infrared spectrum.

### 3.2 MECHANICAL AND ELECTROMECHANICAL DESIGN

The instrument for the IRIS experiment consists of:

- interferometer (cube, detector, mirror drive system, preamplifiers)
- two auxiliary detectors, one for reflected solar radiation, the other for total thermal radiation
- telescope with calibration target (blackbody)
- electronics compartment, containing all electronic circuits except for the preamplifiers in the cube
- mechanical structure to receive the interferometer, the auxiliary detectors, the telescope, and the calibration target, and to provide mechanical strength and thermal protection

The electronics compartment, located separately, is connected to the interferometer and to the auxiliary detectors by a cable.

The mechanical design of the interferometer is modular. The drive unit, the fixed mirror assembly, the detector assembly, and the monochromatic reference

source-detector combination are integral components attached to the optical cube, which houses the beam-splitter and provides mechanical strength and thermal conduction to all components.

The scan mirror is one of the most critical items in the design because it must be moved through a distance of 2 mm with a total angular rotation of less than 2 seconds of arc.

The use of parallel leaf springs to support the mirror was chosen in preference to slides on ways, or pivot-point mounts, since it avoids frictional surfaces undesirable in space applications. The driving force is generated by an electrical current in a moving coil in a strong magnetic field. As Figure 11 shows, the magnetic gap is inside the dual-magnet design, thus minimizing residual magnetic fields on the outside.

Lack of uniformity in drive-mirror speed normally produces catastrophic effects on the wavenumber calibration of interferometers. A resolving power of 400 would require a drive-speed constancy of better than 1 part in 400. Two methods used to eliminate virtually all errors and uncertainties in the mirror motion, and in the subsequent wavelength calibration, are both based on the use of an auxiliary interferometer:

- A monochromatic source (0.5852 micron) feeds the interferometer and generates a sine wave at an auxiliary detector. The frequency of the sine wave is directly proportional to the speed of the mirror. An error signal, derived by a digital comparison of this frequency to a reference frequency generated by a clock, provides fine adjustment of the mirror-drive system. The speed of the drive mirror is therefore feedback-controlled.
- Sampling times of the interferogram are also derived from the reference frequency.

Actually, either of the aforementioned methods would suffice.

### 3.3 OPTICAL DESIGN

The optical design of the interferometer is conventional. The flat mirrors and the detector determine the limiting apertures. The condition of optimum solid angle  $R\Omega = 2\pi$  is fulfilled at the highest wavenumber to be analyzed ( $2000\text{ cm}^{-1}$ ,  $5\mu$ ). The optimum angle is then 8 degrees ( $\pm 4$  degrees) for a resolving power of 400 ( $5\text{ cm}^{-1}$  at  $2000\text{ cm}^{-1}$ ).

The fixed mirror and the scan mirror are made of gold-coated quartz polished to a flatness better than  $0.1\mu$ . Gold was selected because of its stability and its high reflectivity in the infrared. The two-axis mirror mount is machined from a single piece of metal. A differential screw which produces the fine adjustment required also anchors each adjustable plane at three points.

The condensing optic consists of a KRS-5 lens, combined with a gold-coated reflective cone which increases the effective detector area. Dimensions are chosen to provide the 8-degree optimum acceptable angle. This particular optic has sensitivity to almost  $40\mu$ , which will be important for the future development of the instrument in extending the long wavelength limit. The f-number of this system will approach the ideal limit of 0.5.

The bolometer in this design is essentially an integral part of the condensing optic. The detector is a 3.5-mm square masked to a circle of 3.5-mm diameter, having a time constant of 1 millisecond.

The beam-splitter is the most critical item in the optical train. All the rays make two passes through the beam-splitter; hence, all the losses arising in this unit are doubled. Although metallic beam-splitters are preferable from the standpoint of uniformity with wavelength, they have the serious disadvantage that an absorption loss from 25 to 35 percent occurs, depending on the metal used. Dielectric beam-splitters cannot be made uniform with wavelength, but over the wavelength span of interest the efficiency will be at least equal to that of a metallic splitter. The dielectric material selected is germanium, which has the additional advantage of being highly reflective for wavelengths shorter than  $2\mu$  so that most of the reflected visible radiation will not be collected.

The substrate material selected for the beam-splitter and the compensating plate is IRTRAN-4, basically a glass, which can be optically worked in the same fashion as any optical glass. This is a great advantage, because the beam-splitter must be flat to  $1/10$  wavelength of the shortest wavelength of interest. The principal disadvantage of IRTRAN-4 is its long wavelength cut-off at  $20\mu$ .

Other materials investigated for their suitability as beam-splitters (including KBr, KRS-5, CsI, and plastic pellicles) have higher transmission to long wavelengths, but are less suitable in other respects. Further investigations are in process.

The radiation source for the monochromatic reference signal will be the  $0.5852\mu$  neon line, which is quite strong; in conjunction with a suitable interference filter, the signal is suitably monochromatic. Neon was selected because lamps are available in small sizes and very little power is required. The focusing and condensing optics are all glass of conventional and straightforward design. A silicon photovoltaic cell serves as a detector.

The telescope is designed to accept a beam of parallel radiation with an angular aperture of 2.8 degrees and to fill completely the 8-degree field-of-view of the interferometer. The primary and secondary mirror are electroformed for lightweight construction and then gold-coated.

#### 3.4 ELECTRONIC DESIGN

The electronic circuitry for the interferometer package is designed to operate as independently of the spacecraft as possible. The spacecraft supplies the power and command signals necessary to operate the experiment; the electronics subsystem of the experiment processes the interferometer data and presents them to the spacecraft in a digital format. The spacecraft supplies a single command at the beginning of each interferometer frame, but the necessary sequence of events to complete the data frame is generated by means of the interferometer system.

Functions of the interferometer electronics (Figure 12) are:

- To convert the 2400-cps 100v p-p spacecraft power into the voltages required to operate the interferometer instrument
- To provide the necessary power and control to drive the mirror
- To amplify the thermistor bolometer output signal
- To sample the bolometer signal, and to present it in digital form to the spacecraft

The power supply converts the 2400-cps 100v p-p spacecraft power to the voltage levels necessary for operating the interferometer. The power supply includes the necessary regulation ( $\pm 5$  percent) to maintain the voltage to the required accuracy. Three telemetry points are included to monitor:



- Spacecraft input voltage
- 300v  $\pm 0.1\%$  bolometer bias supply
- 12v  $\pm 0.2\%$  reference for mirror drive

The power supply is regulated to 1 percent by feedback to the primary of the power transformer; the 300-volt supply has an additional control that maintains 0.1 percent regulation.

The data channel receives the signal from the thermistor bolometer preamplifier. The signal is band-limited between 10 cps and 110 cps in an electrical filter network. This band-limited signal is then coupled to a switched attenuator and amplified.

The attenuator has two positions, controlled by the level of the preamplifier output voltage: 0-db attenuation and 20-db attenuation. The preamplifier output fed into a comparator generates an output to switch in the 20-db attenuator when the preamplifier output exceeds  $\pm 3.2$  volts, and to switch out the attenuator when the signal falls below  $\pm 0.32$  volts. The gain change is necessary to accommodate the extremely large dynamic range (2000:1) of the input signal from the bolometer preamplifier. The output of the bolometer preamplifier is maintained between 0 and 6.4 volts, a value which is compatible with the analog-to-digital converter.

The function of the data control channel is to:

- Provide the necessary encode pulses to the analog-to-digital converter at proper mirror positions
- Ensure that data points are not transmitted until the mirror velocity has stabilized
- Allow precisely 1708 data points for each data frame

The count-to-128 inhibits the encode pulse for a sufficient time to allow the mirror velocity to stabilize at 0.2 mm/sec. After 128 counts, the 171-cps squarewave is coupled to the analog-to-digital converter as encode pulses. The count-to-1708 circuit counts the number of encode pulses that have been applied to the analog-to-digital converter. After 1708 samples, the mirror drive circuit is de-energized and reset to zero, preparing the experiment for the next frame-initiate command from the spacecraft.

The analog-to-digital converter generates an 8-bit binary word from the bolometer amplifier output. The encode pulse from the data-control channel initiates the digital-to-analog voltage ramp that is compared with the analog voltage from the data channel. When the reference analog voltage matches the data voltage, the digital-to-analog circuit is stopped and the digital word transferred in parallel into the 10-bit shift register as the 8 least significant bits. The ninth bit is generated by the comparator in the data channel designating the amplifier gain; the tenth bit is word synchronization.

At the end-of-code pulse, a gate is opened that allows the 50-kc clock to shift the 10-bit word serially into the spacecraft buffer storage. After 10 counts, the gate between the 50-kc clock and the 10-bit shift register is closed. The tenth bit in the shift register is used for synchronizing the data words in the ground stations.

An additional 7-bit analog-to-digital converter and a set of analog gates are included to sample the low data-rate channels. The analog-to-digital converters are sequentially switched into the spacecraft buffer storage system. The frame-initiate command switches the high data-rate channel into the spacecraft storage, and the end-of-frame pulse switches in the low data-rate channel.

The 400-cps spacecraft clock is coupled to the low data-rate commutator and the 7-bit analog-to-digital converter to serve as switching pulses and encode pulses.

The low data-rate channel contains the housekeeping telemetry and auxiliary measurements of the integrated visible and thermal radiation from the planet; these measurements are transmitted in real time as well as in the low data rate.

The function of the mirror-drive servo-loop is to maintain the mirror velocity constant at 0.2 mm/sec for the 10-second duration of the interferometer data frame. The control system consists of two digital-to-analog voltage ramp generators fed into a summing circuit that drives the mirror drive-power amplifier. The first ramp is a positive-going voltage generated from the 400-cps spacecraft clock; the second ramp is a negative-going voltage generated from the 342-cps neon signal from the interferometer. The output voltages from the two digital-to-analog circuits are weighted so that no signal is applied to the mirror power amplifier when the mirror velocity is constant at 0.2 mm/sec. The loop characteristics of the servo stabilize the mirror velocity at 0.2 mm/sec  $\pm 1$  percent within a fraction of a second after the frame-initiate pulse is received from the spacecraft. After the 1708 data points have been sampled, a pulse from the data-control circuit closes the gate between the

400-cps clock and the digital-to-analog circuits, and resets the counters in the digital-to-analog circuits to zero.

The electronics for the IRIS instrument are designed to perform the functions necessary to control the interferometer and process the data presentation to the spacecraft. The design consists primarily of digital electronics, because of the inherent reliability of digital systems. The digital circuits are constructed of Texas Instrument modules. This subsystem is a self-contained instrument requiring a minimum of external control for the operation of the experiment. A reliability survey will be conducted as one of the system evaluation parameters.

### 3.5 SIGNAL-TO-NOISE RATIO

The peak signal falling on the detector (for zero path difference) is

$$P = \frac{1}{2} N \cdot A \cdot \Omega \cdot \epsilon ,$$

where

P = radiant power (watts)

N = target radiance (watt cm<sup>-2</sup> ster<sup>-1</sup>)

A = effective aperture (cm<sup>2</sup>)

Ω = solid angle (ster)

ε = average optical efficiency

The factor 1/2 accounts for the 50-percent reflection losses inherent in this type of interferometer. The noise at the detector is given by the noise equivalent power (NEP) of a thermistor bolometer, which is approximately

$$\text{NEP} = 1.6 \cdot 10^{-10} \sqrt{a} \sqrt{\frac{\Delta f}{\tau}} ,$$

where

a = area of detector (cm<sup>2</sup>)

Δf = noise bandwidth (cps)

τ = detector time constant (sec)

Additional noise will be contributed by the compensating thermistor ( $\sqrt{2}$ ), noise in the bias supply ( $\sqrt{2}$ ), and preamplifier noise ( $\sqrt{2}$ ). For operation at 260 or 270°K, the NEP is lower; however, this improvement will not be considered here.

The peak signal-to-noise ratio in the interferogram, for zero path displacement, is then

$$\frac{S}{N} = \frac{P}{NEP} \approx 10^9 NA \Omega \epsilon \sqrt{\frac{\tau}{a\Delta f}} .$$

The signal power in the spectral interval  $\Delta\nu$  will be approximately equal to the peak power P times the ratio  $N_{\nu} \Delta\nu \epsilon_{\nu} / N\epsilon$ . In addition, a signal-to-noise improvement factor proportional to  $\sqrt{n/2}$  (n = number of samples per interferogram) is obtained; therefore,

$$\left(\frac{S}{N}\right)_{\Delta\nu} \approx 10^9 N_{\nu} \Delta\nu \epsilon_{\nu} A \cdot \Omega \sqrt{\frac{\tau n}{2a\Delta f}} .$$

Assuming reasonable numerical values for some parameters,

effective aperture A	= 10 cm <sup>2</sup>
solid angle $\Omega$	= 1.57 · 10 <sup>-2</sup> (8°)
optical efficiency $\epsilon \approx \epsilon_{\nu}$	= 0.2
detector time const. $\tau$	= 1 ms
detector area a	= .1225 cm <sup>2</sup>
number of samples n	= 1708
spectral element $\Delta\nu$	= 5 cm <sup>-1</sup>
noise equivalent bandwidth $\Delta f \approx 136$ cps	

the peak signal-to-noise ratio becomes

$$\frac{S}{N} = 2.5 \cdot 10^5 N ,$$

and for a spectral interval

$$\left(\frac{S}{N}\right)_{\Delta\nu} = 3.6 \cdot 10^7 N_\nu .$$

The instrument temperature (270°K) was chosen to give approximately equal signals for the maximum blackbody temperature to be measured (320°K), and for outer space (0°K), which is used as a check of calibration. The maximum radiance between 500 and 2000  $\text{cm}^{-1}$  is about  $8 \cdot 10^{-3}$  watt  $\text{cm}^{-2}$  ster $^{-1}$  (320°K); therefore, the maximum signal-to-noise ratio is about 2000.

Within the spectral intervals, the signal-to-noise ratios depend largely on spectral radiance. A plot of the  $N_\nu$  for various blackbody temperatures is shown in Figures 13 and 14; in both cases, the instrument is at 270°K. However, before the final signal-to-noise ratio can be discussed realistically, errors in the coding process must be taken into account.

The most efficient way to encode is to set one coding step equal to the rms value of the noise in the interferogram. Higher coding accuracy yields insignificant improvement; lower coding accuracy is undesirable. If encoding is performed to 1 part in 2000 of the maximum possible amplitude in the interferogram, the uncertainties introduced by the coding process will equal errors caused by detector noise. The final signal-to-noise value, including the coding error, becomes

$$\frac{S}{N} = 1.7 \cdot 10^5 N \text{ and } \left(\frac{S}{N}\right)_{\Delta\nu} = 2.5 \cdot 10^7 N_\nu .$$

A  $(S/N)_{\Delta\nu}$  equal to unity is obtained for  $N_\nu = 4 \cdot 10^{-8}$ . This value is indicated in Figures 13 and 14. A temperature difference of 1°K should therefore be detectable below 1400  $\text{cm}^{-1}$  (above 7 microns); at 1800  $\text{cm}^{-1}$  (5.5 microns), 3°K corresponds to the noise, and at 2000 (5 microns) only about 6°K.

These numbers were derived for 5  $\text{cm}^{-1}$  resolution. Clearly, numerical smoothing techniques can be applied and resolving power can be traded against accuracy. This operation is done on the ground after the interferogram has been received, so that considerations of this nature do not influence the design of the instrument.

It remains to be shown how a signal-to-noise ratio of 2000 can be obtained in the coding process. The large central peak in the middle of most interferograms is very pronounced; in most cases, the amplitudes in the rest of the interferogram are considerably smaller. An 8-bit word is used to encode on a scale of

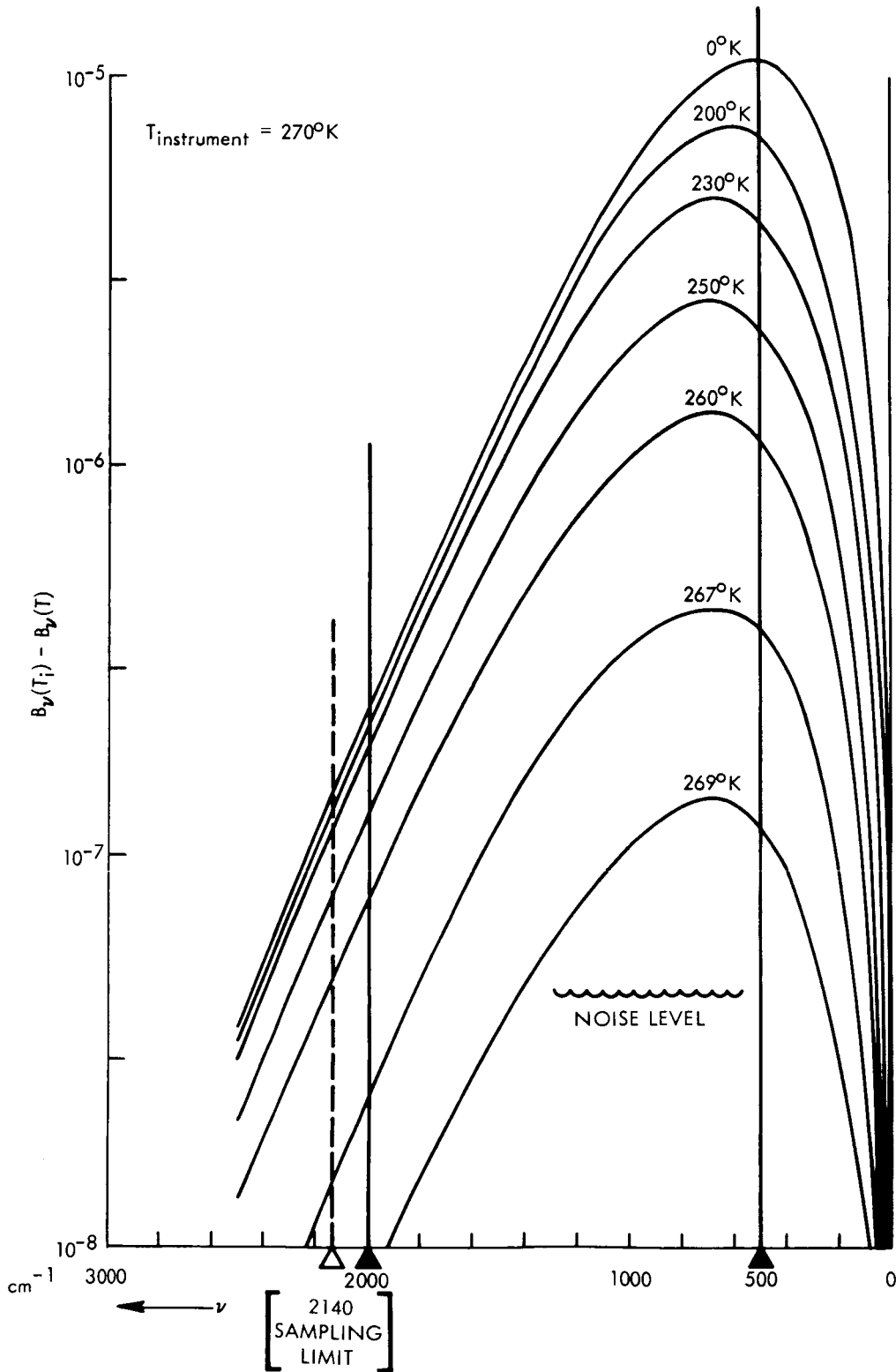


Figure 13—Difference in Spectral Radiance of a Target Colder Than the Interferometer (The curves may also be used to estimate the signal-to-noise ratio.)

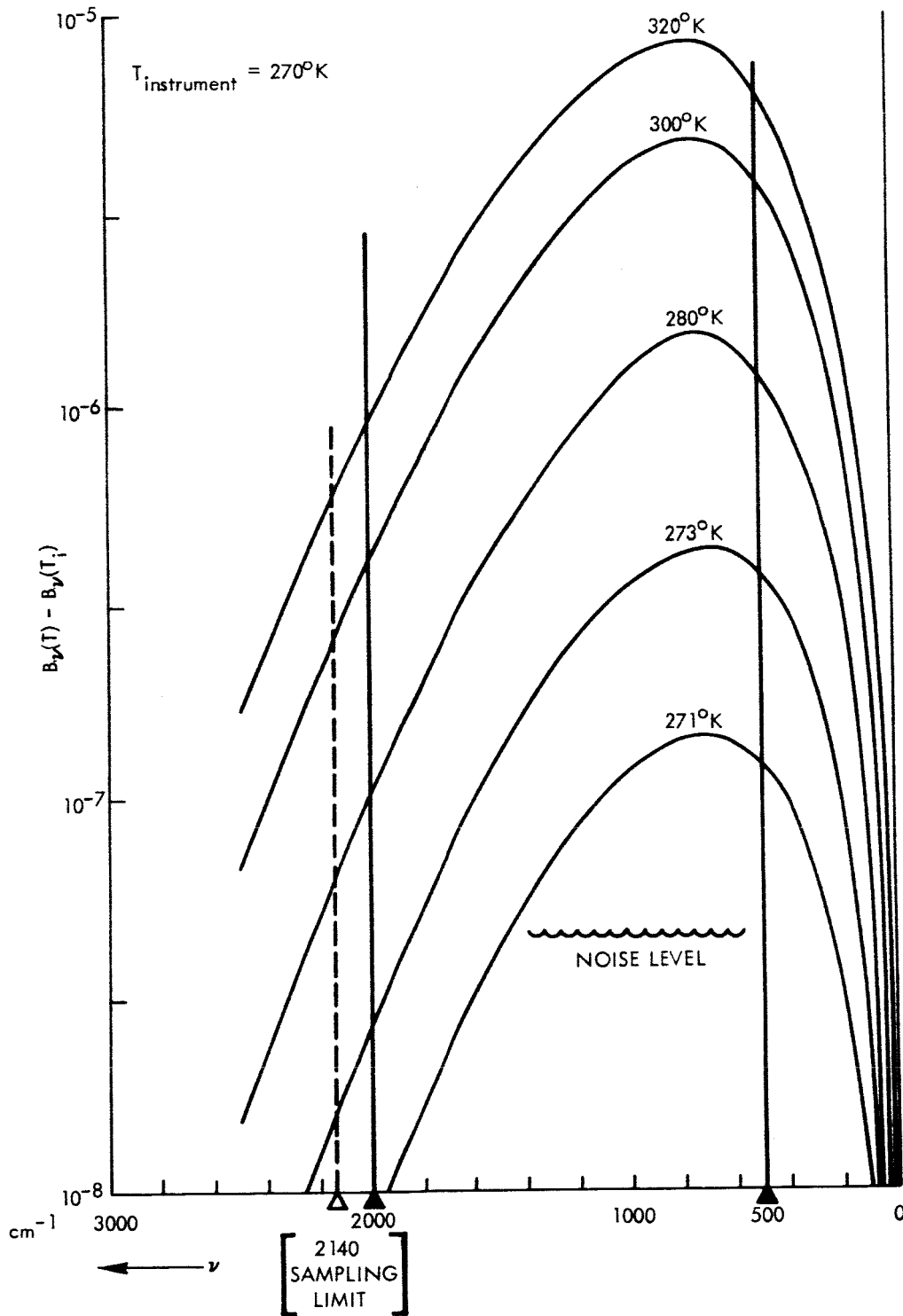


Figure 14—Difference in Spectral Radiance of a Target Warmer Than the Interferometer (The curves may also be used to estimate the signal-to-noise ratio.)

plus and minus 128 levels, or a total of 256. One level is equal to the rms value of the noise. Larger amplitudes are divided by 10 electronically and then encoded. The position of the divide-by-10 circuit is indicated by a ninth bit. This effective dynamic compression maintains full accuracy for most points in the interferogram, but only one-tenth of the full accuracy for all points exceeding a tenth of the maximum possible amplitude. However, the one-tenth value in amplitude is exceeded for only a very small number of data points, compared to the total of 1708 points. The slightly reduced accuracy of a few data points can be shown to have negligible influence on the reproducibility of the spectra.

### 3.6 AUXILIARY MEASUREMENTS

A number of auxiliary measurements will be performed to facilitate better interpretation of the interferograms and to validate the operation of the instrument.

- Reflected Solar Radiation

Reflected solar radiation between 0.5 micron and about 1 micron will be measured by a small radiometer, bore-sighted with the optical axis of the interferometer and having the same field-of-view as the interferometer. The purpose of this measurement is to allow correlation of dark and bright areas on the planet with the interferograms. This instrument will use a silicon cell as a detector, with a time constant of about 10 seconds. A 2-percent relative accuracy and a 10-percent absolute accuracy are sufficient for this measurement.

- Thermal Radiation

Also bore-sighted with the interferometer will be a thermopile having the same spectral response and the same field of view as the interferometer. The purpose of this instrument is to furnish additional calibration of the interferometer during planetary encounter. The time constant of this instrument will also be 10 seconds. A 2-percent relative accuracy and a 10-percent absolute accuracy are likewise sufficient for this measurement.

- Temperature Sensors

Various temperatures will be measured in the optical cube (the temperature of the bolometer mounting, the drive mirror, the beam-splitter mounting, and a point near the entrance aperture) with an accuracy of 0.5°C. These temperature measurements will aid in the proper interpretation of the interferograms. In addition, the temperature of the primary and secondary mirror will be monitored ( $\pm 5.0^\circ\text{C}$ ). The black-body used for calibration purposes before and after planetary encounter will be monitored by two bead thermistors to provide redundancy in this

measurement. Twelve temperature sensors are provided, including the two temperature sensors in the auxiliary radiometers and the two sensors located in the electronics compartment.

- Voltage Measurements

A number of important voltages and execution commands will be monitored to certify proper operation of the instrument. The measured voltages include the bolometer bias voltage, the main power in the optical cube (-12 and -18 volts), and other strategically important voltages in the electronics compartment. A total of 25 auxiliary measurements will be performed.

#### 4. DATA REDUCTION

Computational efforts concerned with the IRIS experiment fall into two major categories: computer simulation of the interferogram, and subsequent analysis to retrieve the optimum amount of information from the received data. The artificially synthesized interferograms will serve as aids for signal-to-noise requirements and in verifying the encoding and digitizing techniques to be applied, as well as in furnishing the basis for the early development of the data analysis techniques to be used. The synthesis of the interferograms has been divided into two phases and the analysis of the data into three phases.

##### 4.1 SYNTHESIS

The purpose of this portion of the study is to simulate the interferogram in order to study the effects of various levels of detector noise, to analyze the possible methods of digital encoding, and to determine the total effect on the ability to recover the underlying frequencies of interest.

The objective of the first phase of the study is a computer program which generates (for specified wavenumbers, instrument and target temperatures, time duration, and sampling rates) the amplitudes of a Fourier series (interferogram) according to the basic instrument characteristics. All computer outputs are formatted, if desired, for plotting offline on an x-y plotter. This part of the program has been completed, and artificial interferograms which were constructed have played an important role in the initial design of the digitization scheme for the instrument.

The first step of the second phase of the interferogram synthesis program is to include the instrument function. The second step is to generate and apply any desired level of detector noise to the signal. The third step is to apply several scaling techniques to find the best one, which will then be used for the

actual instrument. Finally, the digitized version of the interferogram will be formatted to become identical to the output of the physical instrument. The result—the final, simulated interferogram—is again formatted for offline plotting.

#### 4.2 ANALYSIS

The analysis program is being developed concurrently with the synthesis program, because it is essential that the actual interferogram provide the best possible analysis of the data, and of the information extracted. In order to accomplish this, the synthesis and analysis process must be a "closed-loop" learning and improvement system. The resulting analysis program should, therefore, be one which is best fitted to analyze the data from the actual instrument.

The purpose of the first phase of the analysis program is to apply the inverse of the "second-order" effects of the synthesis program; that is, given an interferogram in digital form, the inverse operations of scaling digitizing must be applied, and an apodization function applied, before the frequency analysis is begun.

The second phase of the analysis consists of performing a general Fourier analysis to determine the individual frequency components contributing to the overall composite signal. The Fourier analysis is carried out using both cosine and sine terms.

As a third phase, refinements in the analysis are contemplated. A spectral analysis typically consists of resolving ambiguities and questions that usually cannot be answered by a single analytical technique. The third phase is devoted to the study and development of techniques to be used instead of (or in addition to) the classical, generalized Fourier analysis mentioned above. Techniques to be investigated include auto-regressive analysis—to be used in conjunction with stepwise Fourier analysis—and digital bandpass filters, based on the Laplace transform.

### 5. INSTRUMENT CALIBRATION

To verify the proper operation of the instrument and to assure accuracy in the received data, an in-flight calibration technique will be used. Following is a summary of the final calibrations to be performed on earth, prelaunch check-of-calibration procedures, and in-flight calibration requirements.

### 5.1 PRIMARY CALIBRATION

The primary calibration and check of performance of the instrument will be carried out in a vacuum chamber with cryogenic walls at liquid N<sub>2</sub> temperature. The thermostat of the instrument will maintain the proper operating temperature of about 270°K in the optical cube. A blackbody will be placed in the field-of-view whose temperature can be adjusted between +80°K and +320°K. Interferograms will be taken at 10°K increments. Adjustments of gains, thresholds, etc., will be set at this time. Calibration with the instrument's own reference blackbody will also be checked at this time.

Spectral calibration and resolution will be checked by two methods: First, a polyethylene sheet will be inserted in front of the blackbody in vacuum. Polyethylene has numerous absorption bands of precisely known wavelengths. Second, while in air (or in a chamber with walls and instrument at room temperature), a blackbody at a distance of about 10 m (1 m in the CO<sub>2</sub> chamber) will be kept 10 to 20 degrees above the instrument temperature. The strong Q branch of the 15 $\mu$  CO<sub>2</sub> band, which should be clearly observable in absorption, serves as a wavelength standard. As the mirror speed is derived from the 0.5852-micron neon reference line, this test will verify only proper scan speed. Adjustments will not be necessary.

The field-of-view of the instrument with respect to the mounting interface will be measured on an optical bench. The interferometer will not be operated in the conventional sense for this measurement; the output of the thermistor bolometer will be monitored while a chopped, high-intensity source is moved at a fixed distance. The response will be mapped as a function of the angular position of the source.

### 5.2 CALIBRATION CHECKS DURING ENVIRONMENTAL TESTS

Before and after vibration, during vacuum thermal tests, etc., check of calibration are performed by exposure to blackbodies. In air, blackbodies above room temperature are used; in vacuum tests, blackbodies above and below operating temperatures (+80°K to 320°K). Also, exposure to the electrically-heated reference blackbody which is part of the instrument is performed regularly.

The spectral response is checked by placement of filters (polyethylene or mylar) in front of a blackbody.

The field-of-view is checked in air only, by exposure to a small hot source placed in front of a room temperature background. Readout takes place in the normal operation mode of the interferometer.

### 5.3 CHECK OF CALIBRATION IN THE LAUNCH AREA AND ON LAUNCH PAD

Exposure to the electrically heated, thermostatically controlled reference blackbody will serve as the check of calibration.

### 5.4 CHECK OF CALIBRATION DURING INTERPLANETARY FLIGHT

Two complete interferometer frames will be required for each check of calibration. During the first frame, the reference blackbody will be placed within the field-of-view; this is the normal position of the reference blackbody during flight. The second calibration frame will be taken without the blackbody, with the interferometer viewing outer space. After this, the blackbody will be returned into its normal stowed position. In-flight calibration is required at regular intervals of 15 or 30 days, except during the first week, when one calibration every other day is required.

### 5.5 CALIBRATION AT PLANETARY ENCOUNTER

Shortly before and shortly after planetary encounter, a sequence of two calibration frames is required. The pre-encounter calibration should be as close as possible before encounter but definitely not earlier than 1 hour before. Both pre-encounter calibration frames and post-encounter frames should be stored and transmitted together with the data frames. After encounter, the sequence of the calibration frames will be reversed: first, the sky background will be measured as the planet moves out of the field-of-view of the instrument; then the reference blackbody will be brought in, and the final calibration frame will be taken. Thereafter no further data will be required from the interferometer.

## 6. MISSION PROFILE

### 6.1 PLANETARY TRANSFER

If possible, the instrument will be launched and stowed in the "power on" position. All circuits will be energized and the scan mirror placed in the midrange neutral position. The calibration target (blackbody) will be in front of the telescope so that it seals the instrument thermally; in this position, the blackbody will protect the optical elements during launch and will minimize the heater power necessary to maintain the proper operating temperatures of the instrument (270°K) and the blackbody (285°K). Total electrical power required during this time will not exceed the power required during the data-gathering period (approximately 7 watts). Check of calibration is performed at regular intervals as discussed in 5.4.

The following command and readout sequence constitutes the in-flight calibration:

- Frame-initiate command to obtain one interferogram of the reference target
- Command to move the blackbody out of the field-of-view of the telescope
- Frame command to obtain an interferogram of outer space
- Command to return the blackbody to the normal position in front of the telescope

## 6.2 PLANETARY ENCOUNTER MODE

The planetary encounter mode consists of calibration before and after encounter, as discussed in 5.5, with an intervening data-gathering period. The following sequence of commands and events constitutes the encounter mode:

- Frame-initiate command to obtain one interferogram of the reference target
- Command to move the blackbody to a position which will clear the field-of-view of the telescope
- Frame command to obtain an interferogram of outer space
- Frame command at least every 30 seconds (or, if possible, every 15 seconds) during planetary encounter
- Frame command after the planet has left the field-of-view
- Command to return the blackbody to the normal position in front of the telescope
- Frame-initiate command to obtain interferogram of reference target

After the encounter mode, the data-gathering part of the experiment will be completed and electrical power may be removed from the instrument.

## 6.3 OTHER EXPERIMENT CONSIDERATIONS

- Trajectory—No special requirements
- Fly-by distances—A fly-by distance of 2000 km (closest approach to surface) would be most desirable; at this distance, the interferometer can be used without a telescope. Presently the telescope is designed to

cover the range between 5000 and 10,000 km. An approach distance between 10,000 and 20,000 km would also be acceptable, but would require a new (larger) design of the telescope.

- Fly-by velocity—Low fly-by relative velocity is desirable primarily to minimize the spatial smear during the 10-second time required for each interferogram.
- Aiming point—The aiming point should be chosen to fulfill the following conditions, listed in sequence of importance:
  - (1) Equal chance to observe "dark" and "bright" areas of Mars
  - (2) View of the subsolar point and equatorial regions
  - (3) Scan across the terminator (morning terminator preferred)
  - (4) Observe primarily the illuminated portion of Mars, but to have a chance to see part of the dark side also
- Magnetic cleanliness—No special requirements
- Electrical noise—Only the output circuit of the bolometer and the input to the preamplifier would be sensitive to stray electrical fields. Care will be taken to have proper shielding. The rest of the circuit, which is digital, should be insensitive to stray electrical fields. The noise level which can be tolerated at the electrical interface will be small, but numerical values cannot be specified at this time.
- Acoustical and structural noise—During the 10-second periods of data collection or calibration, the platform should not be exercised. The normal motion of adjustment (hunting) of the spacecraft's control system should not provide problems. The effect of structural noise is not fully known at this time, and specifications of the vibrational environment to which the instrument will be exposed on the spacecraft are urgently needed.
- Interaction and coordination with other experiments—It is strongly suggested that all radiometric experiments be bore-sighted to allow cross-correlation among the data obtained. Simultaneous ground-based observations should be encouraged.

- Spacecraft engineering measurements—No engineering measurements are required from the spacecraft. All auxiliary measurements are part of the interferometer experiment.

## 7. EXPERIMENT-SPACECRAFT INTERFACE

The interface between the experiment and the spacecraft (Figure 15) consists of power input, commands, clock pulses and data signals.

The frame-initiate commands supplied by the spacecraft consist of pulses occurring every 30 or 15 seconds after planet acquisition. The pulse should be about 2 milliseconds in duration and +2 volts in amplitude, with a risetime of about 10 microseconds from a source impedance of about 100 ohms.

The end-of-frame command supplied by the experiment and coupled into the spacecraft is a pulse with an amplitude of 2.5 volts, and a risetime of less than 5 microseconds from a source impedance of about 5K ohms.

The 400-cps clock consists of pulses of a 4-volt amplitude with a 0.3-microsecond risetime and a source impedance of about 100 ohms.

The 50-kc clock coupled from the experiment to the spacecraft will have a source impedance of about 100 ohms and an amplitude of 2.5 volts. The risetime will be on the order of 1 microsecond.

Data output from the experiment will consist of a series of 10-bit digital words, a "one" corresponding to +2.5 volts and a "zero" corresponding to 0 volts. The source impedance in the data channel is 5K ohms.

The real-time data from the thermal and visible channel will consist of a pulse-width about 10 microseconds in duration, with an amplitude of +2.5 volts and a 1-ms risetime.

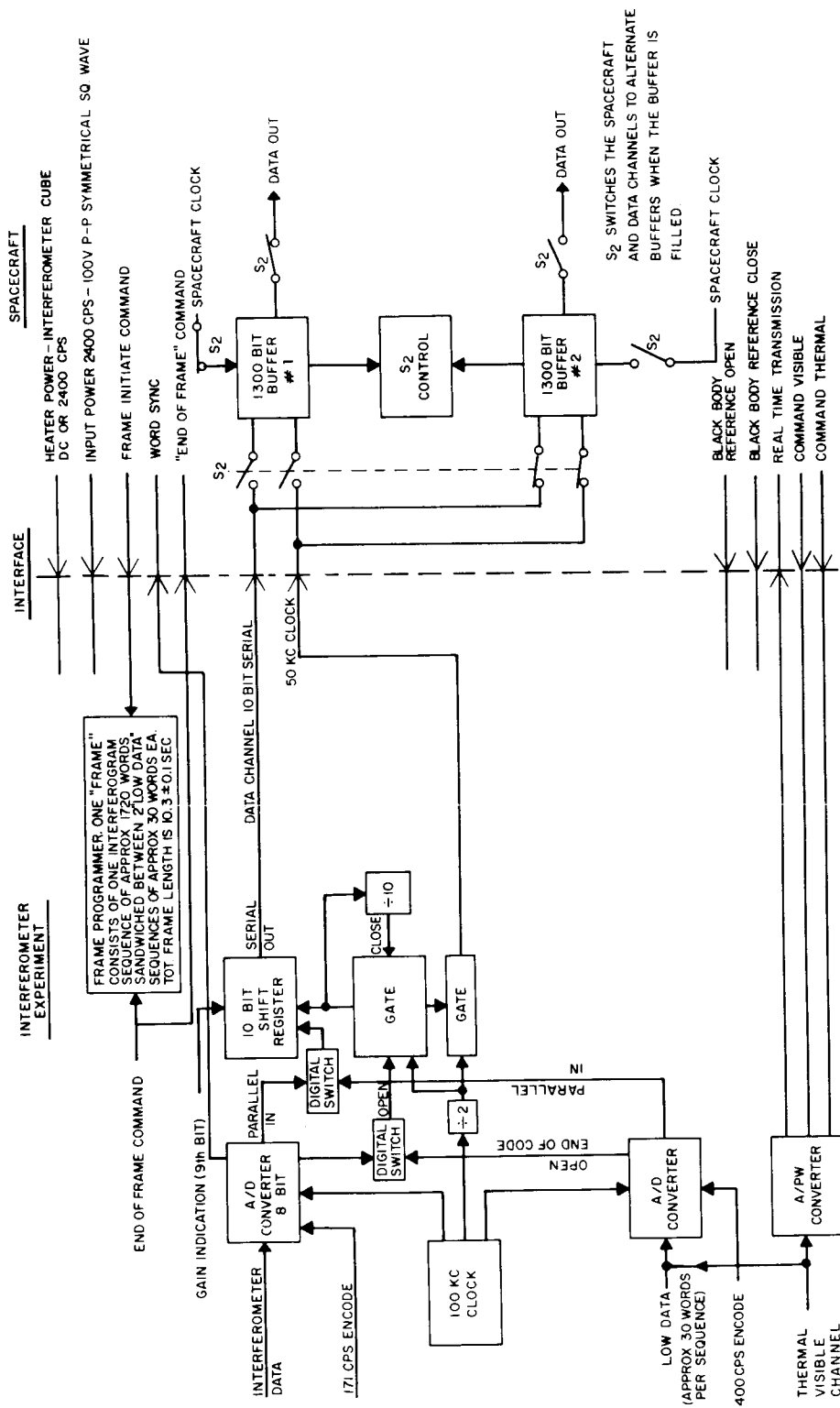


Figure 15--Spacecraft - Experiment Interface

### Design Parameters for Infrared Interferometer

Spectral range	2000-500 $\text{cm}^{-1}$ (5 - 20 $\mu$ ) (possible extension to 300 $\text{cm}^{-1}$ (33 $\mu$ ))
Spectral resolution	5 $\text{cm}^{-1}$ over total range
Travel of drive mirror	0.2 cm
Diameter of effective aperture	3.6 cm
Detector	Thermistor bolometer in conical light pipe
Detector time constant	1 - 2 ms
Duration of interferogram	10 sec
Electrical frequencies at detector	20 - 80 cps
Sampling	Every fourth fringe of monochromatic source 5852.5 Å
Sampling rate	171 samples $\text{sec}^{-1}$
Samples per interferogram	1708
Housekeeping information	25 samples per interferogram
Samples per frame	1733 samples
Frame synchronization	3 words
Words per frame	1736
Bits per word	10
Bits per frame	17360
Calibration frames in vicinity of planet	4

Design Parameters for Infrared Interferometer (continued)

Minimum number of data frames for minimum fly-by speed	40 (every 30 sec) 80 (every 15 sec)
Total number of frames	44 (for 30-sec interval) 84 (for 15-sec interval)
Total number of bits to be stored	$.765 \times 10^6$ (for 30-sec interval) $1.46 \times 10^6$ (for 15-sec interval)
Field-of-view of interferometer	$1.57 \times 10^{-2}$ ster ( $\sim 8^\circ$ )
Field-of-view with telescope	$2 \times 10^{-3}$ ( $\sim 2.8^\circ$ ) (approx. circle of 250 km diameter at 5000 km)
Calibration during interplanetary flight before and after planetary encounter	
a. space	
b. blackbody	
Monochromatic source	Neon lamp plus interference filter
Monochromatic wavelength	5852.5 Å
Detector for monochromatic light	Silicon junction
Frequency of reference signal	684 cps

## REFERENCES

1. Hanel, R. A., and Bartko, F., Radiative Equilibrium in Planetary Atmospheres, NASA TN-G569 (1964)
2. Kuiper, G. P., ed., "The Atmospheres of the Earth and Planets," University of Chicago Press (1952)
3. Sinton, W. M., An Upper Limit to the Concentration of NO<sub>2</sub> and N<sub>2</sub>O<sub>4</sub> in the Martian Atmosphere. Publ. Astron. Soc. Pacific., Vol 73, p. 125 (1961)
4. Kaplan, L. D., "The Spectroscope as a Tool for Atmospheric Sounding by Satellites," Inst. Soc. of Amer. Conf. (Sept. 1960)
5. Wark, D. Q., "On Indirect Soundings of the Stratosphere from Satellites," J. Geophys. Res., Vol. 66, p. 77 (1961)
6. Yamamoto, G., "Numerical Methods for Estimating the Stratospheric Temperature Distribution from Satellite Measurements in the CO<sub>2</sub> Band," J. of Meterol., Vol. 18, p. 581 (1961)
7. King, J. I. F., "Meteorological Inferences from Satellite Radiometry, I," J. Atmos. Sci., Vol. 20, p. 245 (1963)
8. Fleming, H., Twomey, S., and Wark, D. Q., "The Inference of the Vertical Distribution of Atmospheric Parameters from Spectral Measurements," paper presented at the 25th national meeting of the Amer. Meteorol. Soc., Los Angeles (Jan. 1964)
9. Kuiper, G. P., paper presented at 45th American Geophysical Union meeting, Washington, D. C. (April 1964)
10. Lyon, R. J. P., Evaluation of Infrared Spectrophotometry for Compositional Analysis of Lunar and Planetary Soils. NASA Contract (NASA - 49/04) Quarterly Status Report No. 4, Stanford Research Institute (June 1963)
11. Bell, E. E., and Eisner, I. L., Infrared Radiation from the White Sands at White Sands National Monument, New Mexico. Jour. Opt. Soc. of Amer., Vol. 46, p. 303 (1956)
12. Fellgett, P., Spectrometric Interferential Multiples Power Measures Infra-Rouges sur les Etoiles. J. d'Physique et la Rad., Vol. 19, p. 237 (1958)

13. Gebbie, H. A., J. Phys. Radium, Vol. 19, p. 230 (1959)
14. Mertz, L., J. Opt. Soc. Amer., Vol. 46, p. 548 (1956)
15. Connes, J., Rev. d'Opt., Vol. 40, p. 45, 101, 151, 213 (1961)
16. Strong, J., Concepts of Classical Optics, W. H. Freeman and Co., San Francisco (1958)
17. Strong, J., and Vanesse, G. A., Interferometric Spectroscopy in the Far Infrared. J. Opt. Soc. Amer. Vol. 49, p. 844 (1959)
18. Loewenstein, E. V., On the Correction of Phase Errors in Interferograms. App. Optics, Vol. 2, p. 491 (1963)
19. Jacquinot, P., Reports on Progress in Physics, Vol. 23, p. 263 (1960)
20. Connes, J., Recherches sur la Spectroscopie par Transformation de Fourier. Rev. d'Opt., Vol. 40, pp. 45, 101, 157, 213 (1961)

See also:

Öpik, E. J., The Atmosphere and Haze of Mars, J. Geophys. Res., Vol. 65, p. 3057 (1960)

Rea, D. G. and Welch, W. J., The Reflection and Emission of Electromagnetic Radiation by Planetary Surfaces, Space Science Review, Vol. 2, p. 558 (1963)

Steel, W. H., Interferometers Without Collimation for Fourier Spectroscopy. J. Opt. Soc. Amer. Vol. 54, p. 151 (1964)

De Vaucouleurs, G., Physics of the Planet Mars, Faber and Faber, London (1954)

Kiselev, B. A. and Parshin, P. F., Some Distortion in Fourier Spectroscopy. Opt. i. Spektr., Vol. 12, p. 311 (1961)

Meissner, K. W., Interference Spectroscopy. J. Opt. Soc. Amer., Vol. 31, p. 405 (1941)

Strong, J., Interferometry for the Far Infrared. J. Opt. Soc. Amer., Vol. 47, p. 354 (1957)

Kuiper, G. P., "Planets and Satellites," Vol. 3 of The Solar System (Kuiper, G. P. and Middlehurst, B. M., ed.), Chicago: Univ. of Chicago Press (1961)

Urey, H. C. "The Atmosphere of the Planets" in Handbuch der Physik (S. Fluegge, ed.), V. 52:363-418, Berlin: Springer-Verlag (1959)

Sagan, C., and Kellogg, W. W., "The Terrestrial Planets," Ann. Rev. Astron. Astrophys., 1:235-266 (1963)